SLAC-PUB-3316
June 1984
T/E

PARTIAL WAVE ANALYSIS OF THE $\bar{K}^0\pi^+\pi^-$ SYSTEM PRODUCED IN K^- p INTERACTIONS AT 11 *GeV/c**

D. Aston[a], R.K. Carnegie[b], W. Dunwoodie[a], S. Durkin[a,1], P.G. Estabrooks[b], R. J. Hemingway[b], A. Honma[a,2], D. Hutchinson[a], W. B. Johnson[a], P.F.Kunz[a], T. Lasinski[a,3], D.W.G.S. Leith[a], L. Levinson[a,4], R. McKee[c,5], A.C. McPherson[b], W.T. Meyer[a,6], G.K. Oakham[b], B.N. Ratcliff[a], S. Shapiro[a], P.K. Sinervo[a], S. Suzuki[a,7],J. Va'Vra[a,2], S. Williams[a].

ABSTRACT

We have performed a partial wave analysis of the $\bar{K}^0\pi^+\pi^-$ system produced in the reaction K^- p $\rightarrow \bar{K}^0\pi^+\pi^-$n at 11 *GeV/c* and detected in the LASS spectrometer at SLAC. Results from an analysis of $\sim$ 7,600 events in the $\bar{K}^0\pi^+\pi^-$ mass range from 1090 to 2290 MeV/c^2 produced at low t ($|t'| < 0.3$ $(GeV/c)^2$) are described.

The $J^P = 2^+$, 3^- and 4^+ amplitudes show the behaviour expected of the leading K*(1430), K*(1780) and K*(2060) respectively. The behaviour of the $J^P = 1^+$ and 2^- amplitudes can be associated with the $Q_2(1400)$ and the $L(1770)$. The 1^- amplitudes exhibit behaviour which indicates the existence of two resonant states, one near 1400 MeV/c^2 and the other near 1800 MeV/c^2.

A simple Breit-Wigner model is used to fit the leading partial wave amplitudes and to compute branching ratios for the K*(1430) and the K*(1780).

Submitted to *Nuclear Physics B*

---

* Work supported in part by the Department of Energy under contract No. DE-AC03-76SF00515, the National Research Council, Canada and the Natural Sciences and Engineering Research Council, Canada.

[a] Stanford Linear Accelerator Center, Stanford University, P.O. Box 4349, Stanford, California 94305, U.S.A.

[b] Carleton University, Ottawa, Ontario, Canada K1S 5B6.

[c] National Research Council, Ottawa, Ontario, Canada, K1A 0R6.

[1] Present address: University of Pennsylvania, Philadelphia, PA 19104, USA.

[2] Present address: CERN, CH-1211, Geneva 23, Switzerland.

[3] Present address: NASA, Ames Research Center, Mountain View, CA 94040, USA.

[4] Present address: Weizmann Institute of Science, Rehovot 76100, Israel.

[5] Present address: Los Alamos Scientific Laboratory, Los Alamos, NM 87545, USA.

[6] Present address: Iowa State University, Ames, IA 50011, USA.

[7] On leave from Nagoya University, Nagoya, Japan.

1. Introduction

Historically, studies of the $K\pi\pi$ system have been a fruitful source of information on both the natural and unnatural spin-parity strange meson states. Partial wave analyses[1–5] of the diffractively produced $K^{\pm}\pi^{+}\pi^{-}$ system have demonstrated the existence of the $Q_1(1270)$ and $Q_2(1400)$ axial-vector mesons, have provided evidence for the $2^{-}L(1770)$, and have made detailed measurements of the properties of the $K^{*}(1430)$. However, the diffractive channel is dominated by a large Deck background which tends to complicate the analysis and obscure the behaviour of the underlying amplitudes.

Analyses [6–9] of the $\bar{K}^{0}\pi^{+}\pi^{-}$ system produced by charge exchange have shown a consistent picture of the amplitude structure in the $K^{*}(1430)$ region but in general have suffered from low statistics or poor acceptance at $\bar{K}^{0}\pi^{+}\pi^{-}$ masses above 1600 MeV/c^2. These earlier studies have clearly shown the behaviour of the leading $K^{*}(1430)$ and have yielded evidence for the $K^{*}(1780)$, but have not led to any clear understanding of the underlying amplitudes, especially in the region above 1600 MeV/c^2. However, being free of diffractive background, this channel holds the potential of being a source of abundant information on the three-body decays of the strangeness-one states.

We present results from a partial wave analysis (PWA) of the $\bar{K}^{0}\pi^{+}\pi^{-}$ system using events corresponding to the reaction

$$K^{-}p \rightarrow \bar{K}^{0}\pi^{+}\pi^{-}n$$

at 11 GeV/c incident momentum. The data were obtained using the large aperture superconducting solenoid (LASS) spectrometer,[10–13] which is well suited to the study of the $\bar{K}^{0}\pi^{+}\pi^{-}$ system because of its approximately uniform acceptance over a large range of solid angle. In particular, it proved possible to perform a detailed amplitude analysis of the $\bar{K}^{0}\pi^{+}\pi^{-}$ system up to a three-body invariant mass of 1950 MeV/c^2, and a spin-parity decomposition up to a mass of 2290 MeV/c^2.

2. Description of the Experiment

The experiment was performed in an 11 GeV/c RF separated K^{-} beam at SLAC.

The beam particles were tagged as kaons by means of two threshold Čerenkov counters. Scintillation counter hodoscopes and 10 planes of proportional wire chambers with 1 *mm.* wire spacing were located in the beam to measure the momentum and trajectory of the incident kaon.

The LASS spectrometer is shown schematically in figure 1. It consists of a large superconducting solenoid vertex detector followed by a dipole spectrometer. The solenoid generates a 23 *KGauss* field parallel to the beam direction while the dipole field has a dominant vertical component with a field integral of 30 *KGauss−meters* along the beam axis. The solenoid is effective in measuring interaction products which have low momenta ($\lesssim 3-5$ *GeV/c*) and which are not produced too close to the beam axis. High momentum particles ($p > 1.5$ *GeV/c*) close to the beam line are momentum analyzed in the dipole spectrometer.

The 91.6 *cm.* long target filled with liquid H_2 was situated on the axis of the solenoid and was surrounded by a cylindrical proportional wire chamber (PWC) and five cylindrical capacitive-diode readout (CD) spark chambers arranged coaxially, the PWC being the innermost device. Each cylindrical CD chamber had two spark gaps and provided three coordinate measurements. The region downstream of the target was instrumented with three planar CD chambers, 18 PWC planes and three segmented cathode readout foil chambers. Each planar CD chamber consisted of two spark gaps and provided four coordinate measurements. The spark gaps were deadened in the high flux region around the solenoid axis because of their relatively long memory time; nine of the PWC planes had 1 *mm.* wire spacing and 26 by 26 *cm.* active areas and were situated so as to completely overlap the deadened regions of the CD chambers. The remaining nine PWC planes had 2 *mm.* wire spacing and covered the entire bore of the solenoid. A large threshold Čerenkov counter ($\check{C}_1$) filled the downstream aperture of the solenoid and was followed by a 24-segment circular time-of-flight (TOF) array.

The dipole spectrometer was located downstream of the TOF system. A set of eight PWC planes, two CD spark chambers and two magnetostrictive readout (MS) spark chambers instrumented the region between the TOF array and the dipole electromagnet. Four MS chambers, one PWC plane and two segmented scintillator hodoscopes were located downstream of the dipole. Each MS chamber had two

spark gaps and provided four coordinate measurements.

The event trigger for the experiment required two or more charged particles to exit the target, and was defined by requiring: 1) a well-measured incident kaon; 2) that no particle remains in the beam at the end of the spectrometer; 3) two or more hits outside a 3.2 *cm.* square beam hole in the full aperture proportional chamber located 54 *cm.* downstream of the target, and; 4) at least one TOF hit. Additional triggers were mixed with the event trigger to provide a sample of events to study the spectrometer performance.

The raw event sample contained 40 million events, and was reconstructed off-line using the TRIPLEX computer system at SLAC, the computer facility at NRC, Canada, and a set of microprocessors[14] designed to emulate the IBM 370/168 computer. After tracks were found, a topology recognition program classified each event according to the number of charged and neutral vertices. Approximately 31 million events were successfully reconstructed. The remaining 9 million events failed the reconstruction primarily because:

1. the beam track was not reconstructed (usually because two coincident beams were detected);
2. the event buffer was incomplete due to hardware failure in the data acquisition system, or;
3. the number of reconstructed tracks exceeded 15.

The reconstructed events were passed through a software topology filter which selected events consistent with an interaction vertex that had at least two charged prongs and one neutral track (V°) which decayed at least 2 *cm.* downstream into 2 charged secondaries. This filter also required that

$$\sum p_z \geq 9.0\ GeV/c$$

where the sum ran over all charged prongs seen in the event. The requirement that the V° have a $\pi^+\pi^-$ invariant mass consistent with a $\bar{K}^\circ$ produced a data set of 5.2 million events.

The events in this sample were then fit in two different ways:

1. The tracks were geometrically constrained to form a primary vertex with a V° and two charged prongs, with the V° decaying downstream and pointing back to the primary vertex. The inputs to this fit were the measured track coordinates and their uncertainties. The fit took into account energy loss of the particles through the liquid H_2 target but did not place any kinematic requirements on the event. This was called the "geometry-only" fit.

2. The tracks associated with the V° were constrained so that the $\pi^+\pi^-$ invariant mass equalled the $\bar{K}^\circ$ mass. The other charged prongs and the neutral track were constrained to be from a common vertex. This was called the "$\bar{K}^\circ$ mass-constrained" fit. Events which were ambiguous with a Λ° decay hypothesis were also fit with a Λ° mass-constraint.

Only events with a V° and two charged prongs at the primary vertex where kept as $\bar{K}^\circ\pi^+\pi^-n$ candidates. This sample was used as input to a selection program designed to isolate the $\bar{K}^\circ\pi^+\pi^-n$ final state.

3. Selection of the $\bar{K}^\circ\pi^+\pi^-n$ Channel

3.1 Resolution Cuts

Four cuts were made on the data sample to remove poorly measured events:

1. The $\bar{K}^\circ$ mass-constrained fit had to have a confidence level greater than 10^{-3}.

2. The longitudinal momentum balance at the primary vertex had to lie in the range -1.9 to 1.0 GeV/c.

3. The uncertainty of the longitudinal momentum balance at the primary vertex given by the geometry-only fit had to be less than 0.35 GeV/c.

4. The largest percentage error on the momentum of the outgoing tracks had to be less than 8 %.

A number of channels with similar topological configurations to the $\bar{K}^\circ\pi^+\pi^-n$ final state form a background to it. These reactions were examined and removed from the data sample as described below.

3.2 $\bar{K}^\circ$ SELECTION

Approximately 8 % of the V°+ 2-prong sample consisted of Λ° + 2-prong events. Such events had converged Λ° mass-constrained fits in addition to the $\bar{K}^\circ$ mass-constrained fits, and the difference in quality between the $\bar{K}^\circ$ and Λ° mass-constrained fits was then used to identify the decay. Figure 2 shows the $p\pi^-$ invariant mass distribution before and after this selection. No evidence of a Λ° signal remains in the data sample. To allow a simple simulation of the depletion of real $\bar{K}^\circ$ decays in the Monte-Carlo acceptance calculations, an explicit $p\pi^-$ mass cut was performed on the data. The mass cut, 1107 to 1123 MeV/c^2, was somewhat smaller than otherwise necessary to remove the Λ° contamination directly.

Figure 3 shows the $\bar{K}^\circ$ mass distribution after all other cuts had been placed on the data. A final $\bar{K}^\circ$ mass cut was placed on the data from 460 to 535 MeV/c^2.

3.3 CHARGED PRONG SELECTION

A number of background processes existed in the $\bar{K}^\circ$ + 2-prong sample which contained particles other than charged pions at the primary vertex. Such contamination was removed by systematically rejecting each potential background.

The final state $\bar{K}^\circ\phi \rightarrow \bar{K}^\circ K^+ K^-$ comprised 1.3% of the $\bar{K}^\circ$ + 2-prong events. Whenever the invariant K^+K^- mass was below 1049 MeV/c^2 the event was rejected if one of the charged particles was identified as a kaon by the $\check{C}_1$ Čerenkov counter. Figure 4 shows the K^+K^- mass distribution before and after the ϕ contamination was removed.

The fraction of $\bar{K}^\circ$ + 2-prong decays where the two charged prongs were from a γ conversion to e^+e^- was found to be 1.5%. Rejecting events with an e^+e^- invariant mass < 90 MeV/c^2 served to eliminate this background.

Processes with a $K^\circ K^\circ X$ final state (where X was undetected) comprised less than 1% of the $\bar{K}^\circ$ sample. This contamination was removed by rejecting events in which the $\pi^+\pi^-$ invariant mass of the two primary charged prongs was between 470 and 525 MeV/c^2 and the two prongs formed a V° vertex separated from the predicted primary vertex by at least 2 cm.

3.4 NEUTRON SELECTION

The missing mass squared (mm^2) distribution for the final $\bar{K}^\circ\pi^+\pi^-$ event sample prior to any neutron selection is shown in figure 5.

An asymmetric cut was placed on the mm^2 distribution which rejected events outside of a window from 0.383 to 1.100 $(GeV/c^2)^2$. The upper bound was chosen to isolate the $\bar{K}^\circ\pi^+\pi^-$n events from events of the type $\bar{K}^\circ\pi^+\pi^-\Delta^\circ$ when the Δ° decay was not detected in the spectrometer.

The mm^2 resolution of the spectrometer is a complicated function of the measured track parameters, reflecting the difference in track momentum resolution in the solenoid and dipole spectrometer. The distribution shown in figure 5 is consistent with the spectrometer's mm^2 resolution as determined by a Monte-Carlo study of this reaction. A multi-gaussian fit to the distribution in figure 5 with both a neutron and $\Delta^\circ(1232)$ recoiling against the $\bar{K}^\circ\pi^+\pi^-$ system indicated that the Δ° contamination in the neutron sample is less than 4%.

Additional background results from the final states $\bar{K}^\circ\pi^-$p and $\bar{K}^\circ\pi^-$pπ° where, in the latter case, the π° is undetected. Such states can be kinematically ambiguous with $\bar{K}^\circ\pi^+\pi^-$n and are characterized by low 4-momentum transfer from the beam to the $\bar{K}^\circ\pi^-$ system ($t'_{K-K^\circ\pi^-}$) and low nπ^+ invariant mass, which is also a signature of diffractive nπ^+ production where the nπ^+ form a low mass Δ^+ or N*. A "Δ" cut rejecting events with $|t'_{K-K^\circ\pi^-}| \leq 0.2\ (GeV/c)^2$ and $M(n\pi^+) \leq$ 1.8 GeV/c^2 removed over 60% of the $\bar{K}^\circ\pi^-$p contamination and virtually all evidence of diffractive nπ^+ production.

The remaining $\bar{K}^\circ\pi^-$pπ° background appears only at higher $\bar{K}^\circ\pi^+\pi^-$ masses where it becomes necessary to place an additional "pπ°" cut. This cut was done by assuming the event was a $\bar{K}^\circ\pi^-$pπ° final state, and rejecting those events in which the π° was produced backwards in the pπ° rest frame, as measured relative to the direction of the pπ° system in the lab. This effectively removed the $\bar{K}^\circ\pi^-$pπ° events produced at high $t'_{K-K^\circ\pi^-}$ which were not rejected previously. Figure 6 shows the $M^2(n\pi^+)$ distribution for the data before and after these two cuts were made. The enhancement in the nπ^+ invariant mass is completely removed. Figure 7 shows the mm^2 against the $\bar{K}^\circ\pi^-$p system before and after the same cuts. Again

little evidence remains for background from the $\bar{K}^\circ \pi^- p$ and $\bar{K}^\circ \pi^- p \pi^\circ$ final states.

The final data sample consisted of 11,149 events with $|t'| < 1.0\ (GeV/c)^2$. A three-body PWA was performed on the events with $|t'| < 0.3\ (GeV/c)^2$ to study the mass dependence of the partial wave amplitudes of the $\bar{K}^\circ \pi^+ \pi^-$ system. This t' cut left 7,636 events with $M(\bar{K}^\circ \pi^+ \pi^-) < 2300\ MeV/c^2$. The invariant mass distribution of these $\bar{K}^\circ \pi^+ \pi^-$ events is shown in figure 8.

An additional study of the t' dependence of the partial wave amplitudes for $|t'| < 1.0\ (GeV/c)^2$ was performed in the $M(\bar{K}^\circ \pi^+ \pi^-)$ regions around 1430 and 1800 MeV/c^2.

The sensitivity of the data sample with the associated systematic error, taking into account the integrated K^- flux, the density of the H_2 target, the absorption of the beam in the target, and a number of effects related to the efficiency of the analysis software, is 1053 ± 123 events/μb.

4. The Partial Wave Analysis

4.1 Motivation

The Dalitz plot of $M^2(\bar{K}^\circ \pi^-)$ versus $M^2(\pi^+ \pi^-)$ for the entire $\bar{K}^\circ \pi^+ \pi^-$ sample is shown in figure 9. Copious production of $K^*(892)$ and $\rho(770)$ is seen in the data, and $K^*(1430)$ and f(1270) signals are also present. (K^* and K^{**} will be used to refer to the $K^*(892)$ and $K^*(1430)$ respectively). The data sample was divided into three $M(\bar{K}^\circ \pi^+ \pi^-)$ regions, 1010 to 1550, 1550 to 1950 and 1950 to 2300 MeV/c^2 and a Dalitz plot was made for each subset of events. These plots, shown in figures 10-12, illustrate the rich structure in this channel. Because of the strength of the quasi-two-body interactions within the three-meson system, it is natural to employ an isobar model in attempting to understand the dynamics of the $\bar{K}^\circ \pi^+ \pi^-$ system.

4.2 Formalism

The SLAC-LBL three-body isobar program,[15] modified for the study of the $\bar{K}^\circ \pi^+ \pi^-$ system, was used to model the data. The isobar model has been described in considerable detail[16] and so only a brief sketch of the formalism will be presented here.

The $\bar{K}^0\pi^+\pi^-$ system can be described in terms of a superposition of states, each state being characterized by total spin and parity, J^P, helicity, M, and the naturality of the exchange, η. The amplitude for each state is a function of M_{123} and t'. These states decay to quasi-two-body states such as $K^*\pi$ (where the K^* and π are called the isobar and bachelor meson respectively) and subsequently these intermediate states decay to yield the observed $\bar{K}^0\pi^+\pi^-$ system. For a given M_{123} and t', the quasi-two-body state is specified completely by one of the isobar invariant masses (m_i, $i = 1, 2, 3$) and four angles, or equivalently by an expansion in terms of angular momentum eigenstates characterized by total J^P, helicity, M^η, angular momentum, L, between the isobar and bachelor particles, and by the spin, l, of the isobar. This description is schematically shown in figure 13, which shows some of the quantities relevant to the analysis.

Since the polarizations of the target proton and recoil neutron are not observed, an incoherent sum over the amplitudes for the 2 possible spin alignments ϵ of the baryons is made. The production probability for an event ω (described by the isobar invariant mass and 4 angles) is given by

$$\mathrm{p}(\omega) = \sum_{\epsilon,\eta} |\sum_{\tau} \mathrm{A}_{\epsilon\eta\tau} \mathrm{X}_{\eta\tau}(\omega)|^2$$

where the $A_{\epsilon\eta\tau}$ are the partial wave amplitudes, the $X_{\eta\tau}(\omega)$ are the decay amplitudes, and $\tau = \{J^P, M, isobar, L\}$ is the set of variables distinguishing the various amplitudes. Every amplitude (or "wave") is specified by $J^P M^\eta isobar L$, the choice of these values being dictated by the data. The angular dependence of the decay amplitude is determined by J^P, M, L and l while the dependence on m_i, the invariant mass of the isobar, is taken from empirical studies of two-body dynamics. The experimental problem is to determine the behaviour of $A_{\epsilon\eta\tau}$ as a function of M_{123} and t'.

The partial wave amplitudes, $A_{\epsilon\eta\tau}$, were determined using the extended maximum likelihood method. The likelihood function, $\mathcal{L}$, was defined for a set of M_{123} mass bins and maximized independently in each mass bin by varying the $A_{\epsilon\eta\tau}$'s.

This method required a knowledge of the LASS spectrometer's acceptance,

which was obtained through the use of a Monte-Carlo program. Approximately 1.7 million $\bar{K}^0\pi^+\pi^-$ events were generated and tracked through the spectrometer to determine the acceptance as a function of M_{123} for each partial wave used in this analysis. The generated Monte-Carlo events were reconstructed and required to pass the same selection criteria as the data. This ensured, for example, that the effects of the $\bar{K}^0$ and neutron selection were properly taken into account.

4.3 Method of Analysis

The PWA consisted of identifying and measuring the waves needed to describe the observed mass and angular distributions adequately, as functions of $\bar{K}^0\pi^+\pi^-$ mass and t'. The analysis was carried out in a set of mass bins of varying width; the bin width was chosen large enough so that there would be enough events to ensure that the fits remain stable, and yet small enough to reveal the mass dependence of each amplitude.

Table 1 presents the choice of binning for this analysis. The bin size increases with mass to account for the gradual loss of acceptance at higher M_{123}. The data were fit in overlapping bins so that the mass dependence of the amplitudes would be more apparent.

The isobars included in the analysis were:

1. the $K^*(892)$, which was parametrised as a relativistic P wave Breit-Wigner resonance;
2. the $K^*(1430)$, which was parametrised as a relativistic D wave Breit-Wigner resonance;
3. the $\kappa(1350)$, which was described by a K-matrix parametrisation of the $K\pi$ S wave amplitude observed in the two-body reaction $K^- p \to K^- \pi^+ n$;[17]
4. the $\rho(770)$, which was described by a parametrisation of the observed $\pi\pi$ P wave amplitude;[18]
5. the $f(1270)$, which was parametrised as a relativistic D wave Breit-Wigner resonance, and;
6. the $\epsilon(1300)$, which was described by a K-matrix parametrisation of the observed S wave $\pi\pi$ amplitude.[19]

In each mass bin, the same procedure was followed to determine the partial waves needed to describe the data distribution. A large number of random starts, typically 100, were made with a wave set consisting of the waves required by previous three-body analyses of this channel.[6–9] The best solutions (i.e. the solutions with the highest likelihood) in each mass bin were retained. Then an additional wave (from a set of possible waves described below) was added to the wave set and another series of random starts was performed to find the best solutions with this augmented wave set. At each stage, the solutions were examined to determine whether any one wave amplitude had become statistically insignificant. Such waves were subsequently removed and the fitting procedure repeated.

When all the possible waves had been added to the wave set individually, a new wave set was created which included any new waves that had made sizable increases in the likelihood of the fit. The fitting procedure was again repeated, and additional waves were added and rejected. After an exhaustive study had been made of the wave sets in each bin, the sets in adjacent bins were examined. Any differences were reconciled by demanding a significant amplitude of each wave over several adjacent bins. The final solutions were chosen by requiring reasonable continuity of the wave amplitudes across several M_{123} bins.

The extra waves considered in this algorithm depended on the mass region being fit. For bins with $M_{123} < 1570\ MeV/c^2$ all possible waves with $J \leq 2$ were considered; larger J values were tried in the mass region above 1570 MeV/c^2, but waves with $J = 3$ were found to be sizable only above 1650 MeV/c^2, and waves with $J = 4$ were required only above 1950 MeV/c^2.

The wave set used to obtain the final amplitudes is shown in figure 14. Below a mass of 1800 MeV/c^2, the solutions were quite stable and displayed only one ambiguity that had to be resolved using criteria other than those described above. Above this mass, the fitted amplitudes became unstable; this comes about in part because the cuts required to remove the $\bar{K}^0\pi^-\,p\,\pi^0$ contamination become increasingly severe, reducing the number of available events; however it is also due to the fact that the number of waves (and hence the number of parameters) needed to describe the data adequately increased rapidly as a function of M_{123}. These effects place an additional burden on the robustness of the fitting algorithm, as well as the

model itself.

These problems resulted in an inability to discriminate between several different high-spin waves in the mass region above 1800 MeV/c^2. In particular, ambiguities arose between the 4^+, 3^+ and 3^- waves decaying into the $K^{**}\pi$ channel. Below a mass of 1950 MeV/c^2, the 3^+ wave was removed as it showed the most erratic behaviour, the lowest intensity on average, and had the least effect on the likelihood of the fits. These ambiguities did not affect the behaviour of the other waves including the $3^- K^*\pi$ and $3^-\rho K$ waves. In the region above 1950 MeV/c^2 a unique isobar decomposition of the data into partial waves could not be achieved but the J^P decomposition of the cross section was feasible up to 2300 MeV/c^2.

One ambiguity remained in the solutions below 1800 MeV/c^2. In the region between 1300 and 1600 MeV/c^2, two discrete branches in the wave amplitudes were present, labelled Branch *I* and Branch *II*. The differences between these two branches were confined to the $\eta-$ waves and related to the behaviour of the $2^+ K^*\pi$, the $1^- K^*\pi$ and the $1^-\rho K$ waves. No criterion was found which absolutely ruled out either of these branches. However a number of arguments are presented in section 4.8 in favor of Branch *I*, based on the physical interpretation of the amplitudes.

The resulting partial wave amplitudes are expressed in terms of the acceptance corrected number of events attributed to each wave. The waves divide into two sets of opposite naturality ($\eta \pm$), each set being composed of mutually coherent amplitudes. A reference wave must be chosen for each η in order to define the relative phases of the amplitudes. The $1^-0^- K^*P$ amplitude was used as the reference wave for the $\eta-$ waves and the $1^+0^+ K^*S$ ($1^+0^+\epsilon S$) amplitude used as a reference for the $\eta+$ waves in the region below (above) 1550 MeV/c^2. The observed phase of a wave is only meaningful, however, when the amplitude is large enough to create significant interferences with the other waves of the same naturality. For small amplitudes, the phase is unmeasurable and such phase points are not shown in the accompanying figures.

4.4 Total J^P Intensities

Figures 15 and 16 show the coherent sums of the intensities of each of the J^P's

needed to describe the data:

1^- The 1^- intensity is very strong through most of the mass region accessible to this analysis. It rises swiftly above 1300 MeV/c^2 to a plateau above 1400 MeV/c^2, followed by another rise to a peak around 1800 MeV/c^2. In the region around 1800 MeV/c^2 this term is the largest single contribution to the total intensity, dwarfing the 3^- signal.

2^+ The sum of the 2^+ waves shows a large peak with little background in the region of the well-established $K^*(1430)$. An interesting feature is the definite rise in the intensity above 2000 MeV/c^2. This feature is insensitive to the high-mass ambiguities discussed in the previous section, and confirms a similar effect seen in two of four solutions in an analysis of the $K^-\pi^+$ channel.[13]

3^- The 3^- intensity turns on rapidly above 1600 MeV/c^2, reaching a peak around 1800 MeV/c^2 with a substantial dip, followed by some indications of a subsequent increase in amplitude above 2100 MeV/c^2. The peak around 1800 MeV/c^2 is associated with the 3^- $K^*(1780)$ which has been observed in previous analyses of the strange meson channels.

4^+ The 4^+ intensity is only appreciable above 1800 MeV/c^2. As mentioned in the previous section, the partial wave analysis becomes increasingly unstable above 1800 MeV/c^2 and so a detailed isobar decomposition of the 4^+ signal is not presented in this paper. The 4^+ intensity shows an enhancement around 2100 MeV/c^2. This effect can be associated with the 4^+ $K^*(2060)$ previously observed in the $K\pi$ channel.[11,13,20]

0^- There is only one wave contributing to this intensity, the $0^-0^+\epsilon S$. A detailed discussion of this wave is presented below.

1^+ The 1^+ intensity is quite large over the entire mass region and shows no definite structure.

2^- This intensity shows a peak around 1750 MeV/c^2 with little structure elsewhere. It is dominantly from a single wave, the $2^-0^+ K^{**}\pi S$ and a detailed discussion is deferred to the next section.

3^+ The 3^+ intensity is measurable above 1900 MeV/c^2 but does not show any definite structure.

4.5 THE η – WAVE AMPLITUDES

The intensities of the η – waves are shown in figures 17-20. The Branch *I* solutions are plotted as solid points, and these will be described first.

The $1^-0^-\mathrm{K}^*P$ amplitude is large through the entire mass region and was used as the reference wave for the η – amplitudes. It shows a dramatic peak around 1400 MeV/c^2, falling quickly to approximately half its peak value. The $1^-0^-\rho P$ amplitude is only significant above 1400 MeV/c^2, growing quickly with increasing $\bar{\mathrm{K}}^0\pi^+\pi^-$ mass until it peaks around 1800 MeV/c^2. The $1^-0^-\rho P$ amplitude is the largest partial wave in the 1800 MeV/c^2 region and is the dominant contribution to the second bump seen in the $\bar{\mathrm{K}}^0\pi^+\pi^-$ invariant mass distribution of figure 8. The $1^-0^-\rho P$ phase relative to the $1^-0^-\mathrm{K}^*P$ wave moves slowly backward around 1500-1600 MeV/c^2 and then remains constant through the 1800 MeV/c^2 region. The coherent sum of these two waves results in the large 1^- cross section shown in figure 15.

The $J^P = 2^+$ waves are shown in figures 18 and 19. A strong resonant peak is observed in the $2^+0^-\mathrm{K}^*D$, $2^+0^-\rho D$ and $2^+1^+\mathrm{K}^*D$ intensities at the mass of the $\mathrm{K}^*(1430)$. The $2^+1^-\mathrm{K}^*D$ intensity shows no hint of structure, but is very small. The $2^+0^-\mathrm{K}^*D$ phase measured relative to the $1^-0^-\mathrm{K}^*P$ wave is almost constant through the region where the 2^+ intensities are displaying resonant behaviour, implying that the $1^-0^-\mathrm{K}^*P$ absolute phase is rotating at approximately the same rate as the phase of the $2^+0^-\mathrm{K}^*D$. No other structure is observed in these waves up to 1950 MeV/c^2.

The $3^-0^-\mathrm{K}^*F$, $3^-0^-\rho F$ and $3^-0^-\mathrm{K}^{**}D$ amplitudes are shown in figure 20. The $3^-0^-\mathrm{K}^*F$ intensity shows a peak at 1800 MeV/c^2 which is indicative of the $3^-\mathrm{K}^*(1780)$. The $3^-0^-\mathrm{K}^*F$ phase measured relative to the $1^-0^-\mathrm{K}^*P$ wave shows little motion. Assuming that the $3^-0^-\mathrm{K}^*F$ amplitude is dominated by the resonance contribution, this would imply that the $1^-0^-\mathrm{K}^*P$ and $1^-0^-\rho P$ absolute phases are also advancing rapidly. The $3^-0^-\rho F$ intensity is substantially smaller in magnitude and does not display a clear resonant structure. The $3^-0^-\mathrm{K}^{**}D$ intensity is also small in this region indicating that the $\mathrm{K}^*(1780)$ does not couple strongly to the $\mathrm{K}^{**}\pi$ system.

The Branch *II* solutions for the $1^-0^-\,\mathrm{K}^*P$, $1^-0^-\rho P$ and $2^+0^-\,\mathrm{K}^*D$ waves are shown as open points in figures 17 and 18. In the 1^- waves, the two branches differ in their isobar decomposition into $\mathrm{K}^*\pi$ and $\rho\mathrm{K}$ final states. The Branch *II* solutions show an enhancement in the $1^-0^-\rho P$ intensity around 1450 MeV/c^2 with no notable structure in the $1^-0^-\,\mathrm{K}^*P$ wave. In the case of the Branch *II* solution to the $2^+0^-\,\mathrm{K}^*D$ amplitude, the entire lineshape appears to be shifted ~ 20 MeV/c^2 higher in mass and the magnitude of the K*(1430) peak is reduced. The relative phase of the $2^+0^-\,\mathrm{K}^*D$ is also shifted by $\sim 180°$ indicating that the sign of the interference between this wave and the $1^-0^-\,\mathrm{K}^*P$ reference wave has changed.

4.6 The η + Wave Amplitudes

The η + partial wave amplitudes are shown in figures 21 and 22. The $0^-0^+\epsilon S$ intensity shows a broad hump at 1400 MeV/c^2 and gradually decreases in intensity. There is a fluctuation in the amplitude at 1600 MeV/c^2. It is possible to replace this wave with the $0^-0^+\,\kappa S$ amplitude and achieve a reasonable fit to the data with a small overall decrease in likelihood. The other partial wave amplitudes are not affected by such a replacement and the behaviour of the $0^-0^+\,\kappa S$ wave does not differ markedly from the observed behaviour of the $0^-0^+\epsilon S$ amplitude. These conclusions are also insensitive to details of the ϵ and κ sub-mass dependences.

The $1^+0^+\,\mathrm{K}^*S$ intensity shows a broad enhancement at 1400 MeV/c^2 with no structure in the higher mass region. The enhancement is attributed to the production and decay of the Q_2(1400) resonance which is seen in the diffractively produced $\mathrm{K}\,\pi\pi$ final states.[1,2] The intensity of this wave falls off smoothly at higher masses.

The $1^+0^+\rho S$ intensity shows no significant structure in the same region and vanishes rapidly above 1500 MeV/c^2. There is little evidence of the Q_1(1270) which is produced with the Q_2 in the diffractive reaction.

The $1^+0^+\epsilon S$ intensity rises rapidly above 1500 MeV/c^2 with a discontinuity at 1800 MeV/c^2. It was not possible to replace this wave with the $1^+0^+\,\kappa S$ amplitude without a serious decrease in the likelihood of the fit.

The $2^-0^+\,\mathrm{K}^{**}S$ intensity in figure 21 shows evidence for the 2^-L(1770) meson,

which has been studied in the diffractive $K\pi\pi$ channel.[1] The $K^{**}\pi$ is the only significant 2^- wave below 1950 MeV/c^2; the $2^-0^+ f S$ amplitude is small in this region and does not display any significant structure.

4.7 Production Angular Distributions

To measure the production properties of the partial waves, the data in the two mass ranges 1350 to 1510 MeV/c^2 and 1710 to 1890 MeV/c^2 were analyzed in four t' bins as shown in table 2. The results of this analysis for the major partial waves are shown in figure 23. The solutions in the low mass bin are shown as solid points and lines, and the high mass bin solutions are represented by the open points and dashed lines. The Branch I solutions are displayed for the $1^-0^- K^*P$ and $2^+0^- K^*D$ waves (solid dots), and the Branch II solution is shown for the $1^-0^-\rho P$ (solid triangles). The other relevant t' dependences cannot be measured because the corresponding amplitudes are too small.

The intensities exhibit approximately exponential t'-dependence with the fitted slope parameters listed in table 3. The steep t' dependence of the $2^+0^- K^*D$, $3^-0^- K^*F$ and $1^-0^-\rho P$ partial waves contrasts sharply with the much flatter t' dependence of the $1^+0^+ K^*S$ and $1^-0^- K^*P$ waves in the low mass bin.

4.8 Choice of Solution Branch

The ambiguity between Branch I and II was resolved by noting the following features of the two sets of solutions:

1. The peak in the $2^+0^- K^*D$ amplitude is shifted higher in mass in the Branch II solutions. This would imply an anomalously high mass for the K*(1430), and disagrees with the lineshapes of the other 2^+ waves. Therefore, a consistent description of the K*(1430) is not possible with the Branch II solutions.
2. The t' dependence of the Branch II $1^-0^-\rho P$ wave in the 1430 MeV/c^2 region is steep, indicating that it is produced with a substantial π-exchange component, and hence that the amplitude has a strong $K\pi$ coupling. An analysis of the $K^-\pi^+n$ final state[13] shows very little elastic P wave amplitude in the 1450 MeV/c^2 region. There is no simple way of reconciling the behaviour of the $1^-0^-\rho P$ amplitude in the absence of a comparable signal in the $K\pi$ P wave. The Branch I $1^-0^- K^*P$ amplitude does not contradict

the $K\pi$ data as it appears to be produced by the exchange of a heavier object.

In view of these inconsistencies, the Branch *II* solutions are rejected as a physical description of the $\bar{K}^0\pi^+\pi^-$ system.

4.9 Interpretation of the 1^- Amplitudes

The $1^-0^-\,K^*P$ wave shows a sharp peak around 1400 MeV/c^2, remaining quite strong through 1800 MeV/c^2. The phase of the $2^+0^-\,K^*D$ relative to the $1^-0^-\,K^*P$ suggests that the $1^-0^-\,K^*P$ amplitude is undergoing resonant motion in the 1400 MeV/c^2 region. The phase of the $3^-0^-\,K^*F$ relative to the $1^-0^-\,K^*P$ wave suggests that the phase of the $1^-0^-\,K^*P$ is also resonant in the 1800 MeV/c^2 region. The t' dependences of this amplitude at 1400 and 1800 MeV/c^2 are quite different implying different production mechanisms in the two mass regions.

The $1^-0^-\rho P$ amplitude shows a strong resonant peak at 1800 MeV/c^2 with a constant phase relative to the $1^-0^-\,K^*P$ wave through this region. The t' dependence of this wave indicates that it is being produced by a π-exchange mechanism. There is no evidence of resonant structure in the $1^-0^-\rho P$ wave around 1400 MeV/c^2.

A model incorporating two 1^- resonances, one near 1400 MeV/c^2 and the other near 1800 MeV/c^2, successfully describes the features of these 1^- amplitudes.[21] The lower mass state couples only to $K^*\pi$ and not to ρK and $K\pi$, the lack of $K\pi$ coupling being substantiated by the weak t' dependence of the $1^-0^-\,K^*P$ intensity around 1400 MeV/c^2 and by the negligible $K\pi$ P wave amplitude[13] in the same mass region. The enhancement in the $K\pi$ P wave[13] around 1750 MeV/c^2 is associated with the two-body decay of the higher mass state. This state decays into ρK, $K^*\pi$ and $K\pi$, the steeper t' dependence of the $1^-0^-\rho P$ and $1^-0^-\,K^*P$ intensities in the 1800 MeV/c^2 region confirming the coupling of this object to the elastic channel. In the context of light quark spectroscopy, it is natural to interpret the lower mass state as being the first radial excitation of the $K^*(892)$, and the higher mass state as the 1^- member of the leading triplet containing the $3^-\,K^*(1780)$. A detailed discussion of the 1^- amplitudes has been presented in reference 21.

5. Mass Dependent Fits to the 2^+ and 3^- Amplitudes

The 2^+ and 3^- amplitudes yield new measurements of the properties of the $K^*(1430)$ and $K^*(1780)$ states. To extract the parameters for these resonances a set of mass-dependent fits were made to the Branch *I* amplitudes. The relativistic Breit-Wigner line-shape[22]

$$\frac{d\sigma_n^j}{dM} = \mathrm{N}\left[\frac{\sqrt{M\,M_n\,\Gamma_n^j}}{M^2 - M_n^2 - i\,M_n\,\Gamma_n^{tot}}\right]^2 \tag{1}$$

was used to parametrise the resonant behaviour of the *nth* resonance decaying into the *jth* isobar; N is a normalization constant, M is the three-meson invariant mass, and M_n is the resonant mass. The mass-dependent partial width Γ_n^j is parametrised as

$$\Gamma_n^j = \frac{\left(\gamma_n^j\right)^2 BF_{L_n^j}(Q^j)}{M_n\,BF_{L_n^j}(Q_n^j)}\left(\frac{Q^j}{M}\right). \tag{2}$$

Q^j and Q_n^j are the magnitudes of the 3-momenta of the bachelor meson evaluated in the 3-meson center of mass for masses M and M_n, respectively, L_n^j specifies the angular momentum eigenstate of the isobar-bachelor system, $BF_{L_n^j}(Q)$ is a Blatt-Weisskopf barrier factor which behaves as $Q^{2L_n^j}$ at threshold and approaches a constant as $Q \to \infty$, and γ_n^j is a constant with units of energy which is directly related to the partial width of the resonance. The total width of the resonance Γ_n^{tot} is approximated by a constant independent of Q and M.

The partial wave amplitudes measured in non-overlapping bins were fit to a number of models which predict the behaviour of a set of partial waves as a function of $M(\bar{\mathrm{K}}^0\pi^+\pi^-)$. The best estimate of the parameters of each model was obtained by minimizing the χ^2 for the model. The χ^2 was computed by using the full error matrices from the fits to the partial waves in each mass bin. The model predictions for the partial wave intensities and phases were properly averaged over the full mass bin to take into account the finite bin widths.

5.1 THE $J^P = 2^+$ WAVES

The 2^+ waves $2^+0^-\,\mathrm{K}^*D$, $2^+0^-\rho D$ and $2^+1^+\,\mathrm{K}^*D$ were fit to a common resonant lineshape, with each wave having an independent background contribution. The background amplitudes were allowed to have a linear mass dependence with a constant phase relative to the real part of the resonant amplitude. A change of $\sim 70^\circ$ is observd in the phase of the $2^+0^-\,\mathrm{K}^*D$ wave relative to the $2^+0^-\rho D$ wave, whereas no relative phase change is expected if these two waves are dominated by the $\mathrm{K}^*(1430)$ resonance. A similar effect has been observed in the diffractive $\mathrm{K}^-\pi^+\pi^-\mathrm{p}$ channel[1] and is attributable in both cases to a $\rho-\omega$ interference effect. Such an explanation is consistent with the observed $\pi^+\pi^-$ mass distribution in the present data sample. Therefore, the $2^+0^-\,\mathrm{K}^*D$ and $2^+0^-\rho D$ relative phase was not used in the coupled 2^+ fit. The phase of the $2^+1^+\,\mathrm{K}^*D$ measured relative to the $1^+0^+\,\mathrm{K}^*S$ was also not used because the behaviour of the reference wave was not modeled.

The curves superimposed on the amplitudes in figures 18 and 19 show the results of the fit. The quality of the fit is reasonable with a χ^2 of 10 for four degrees of freedom. The mass and width of the resonance are $1433 \pm 6 \pm 10$ and $131 \pm 24 \pm 20$ MeV/c^2 respectively. The first error corresponds to the statistical uncertainty and the second is an estimate of the systematic uncertainty due to the variation of the fitted parameter with the choice of background parametrisation. The ratio of the number of events decaying into $\rho\mathrm{K}$ and $\mathrm{K}^*\pi$ states (summed over $M^\eta = 0^-, 1^+$) is $.313 \pm .062 \pm .025$. Taking into account the different isospin weights of the two final states, the measured $\rho\mathrm{K}\,/\,\mathrm{K}^*\pi$ branching ratio for the $\mathrm{K}^*(1430)$ is $.417 \pm .082 \pm .033$.

5.2 THE $J^P = 3^-$ WAVES

The $3^-0^-\,\mathrm{K}^*F$ intensity (figure 20) was fit to a resonant lineshape to determine the mass and width of the $\mathrm{K}^*(1780)$. The fitted mass and width are $1790 \pm 20 \pm 20$ MeV/c^2 and $138 \pm 18 \pm 40$ MeV/c^2, respectively. The large systematic error on the resonant width arises from its sensitivity to the background assumptions employed in the fit. The model prediction for the lineshape of the $3^-0^-\,\mathrm{K}^*F$ is shown in figure 20.

The $3^-0^-\rho F$ and $3^-0^-\mathrm{K}^{**}D$ intensities show little evidence of the $\mathrm{K}^*(1780)$ coupling to these two isobars, so that a measurement of the $\mathrm{K}^*(1780)$ $\rho\mathrm{K}/\mathrm{K}^*\pi$ and $\mathrm{K}^{**}\pi/\mathrm{K}^*\pi$ branching ratios is not possible. Conservative upper limits on these ratios were established by fitting a Breit-Wigner resonance to the intensities of the $3^-0^-\mathrm{K}^*F$, $3^-0^-\rho F$, and $3^-0^-\mathrm{K}^{**}D$ amplitudes, assuming no background contributions below the fitted resonance mass. The results of the fit are used to quote 95 % confidence level upper limits on the branching ratios. The upper limit on the $\rho\mathrm{K}/\mathrm{K}^*\pi$ branching ratio, after correcting for isospin, is .77. The upper limit on the $\mathrm{K}^{**}\pi/\mathrm{K}^*\pi$ branching ratio, after correcting for the $\mathrm{K}^*(1430)$ branching fraction into $\mathrm{K}\pi$[13], is 1.78. Although these are weak upper limits, they are the first measurements of these branching ratios and will be used in the next section to place a lower limit on the total of the unseen $\mathrm{K}^*(1780)$ decay modes.

5.3 Branching Ratios Relative to $\mathrm{K}^-\pi^+$

Reference 13 describes the results of a PWA of the $\mathrm{K}^-\pi^+$ system using the data on the reaction

$$\mathrm{K}^-\mathrm{p} \rightarrow \mathrm{K}^-\pi^+\mathrm{n},$$

also obtained in the present experiment. These results can be combined with those of the present analysis to determine the $\mathrm{K}^*\pi/\mathrm{K}\pi$ and $\rho\mathrm{K}/\mathrm{K}\pi$ branching ratios for the $\mathrm{K}^*(1430)$, and the $\mathrm{K}^*\pi/\mathrm{K}\pi$ branching ratio for the $\mathrm{K}^*(1780)$, this being the first measurement of these quantities using results from a single experiment. The simplest way to compute these branching ratios is to determine the $\mathrm{K}^-\pi^+$ production cross sections for the D and G waves, which can then be directly compared to the partial wave intensities measured in the $\bar{\mathrm{K}}^0\pi^+\pi^-$ PWA, using the effective experimental sensitivities for the two final states.

The D wave and G wave amplitudes in reference 13 are the pure $\mathrm{K}\pi$ elastic scattering amplitudes and are related to the production amplitudes by the exchange model employed in the analysis. After computing the acceptance corrected number of produced events corresponding to the D and G waves, these quantities have to be corrected for the different t' bins used in the two analyses, using the measured t' dependences of the waves. The different helicity amplitudes for each spin-parity

wave * are summed together to give the total number of events corresponding to the $K\pi$ D and G waves. The effective sensitivity for the $K^-\pi^+$ channel is then used to determine the number of the K*(1430) and K*(1780) events decaying into the $K\pi$ final state.

The branching ratios are summarized in table 4. The quoted errors include both statistical and systematic contributions. These ratios have been corrected for the $\bar{K}^0$ visibility and the isospin weights of the different charge modes. The K*(1430) $K^*\pi/K\pi$ branching ratio of $.44 \pm .09$ is one standard deviation lower than the Particle Data Group estimate of $.517 \pm .056$.[23] The $\rho K/K^*\pi$ branching ratio of $.42 \pm .08$ agrees well with the results of previous high-statistics partial wave analyses[1,6,9] of $K\pi\pi$ data.

The K*(1780) $K^*\pi/K\pi$ branching ratio is $1.09 \pm .26$ and is the first measurement of this quantity. Since the dominant three body decay mode is $K^*\pi$ and the measured elasticity of the K*(1780) is $.16 \pm .01$[13], this state must have a large partial width into higher multiplicity channels. By combining the measurements of the K*(1780) elasticity, the $K^*\pi/K\pi$ branching ratio and the upper limits on the $\rho K/K^*\pi$ and $K^{**}\pi/K^*\pi$ branching ratios, a 95 % confidence level lower limit of .22 can be placed on the K*(1780) branching fraction into final states other than $K\pi$, $K^*\pi$, ρK and $K^{**}\pi$. Since the present data shows no clear evidence for the K*(1780) decay into ρK or $K^{**}\pi$, the $K\pi$ elasticity and $K^*\pi/K\pi$ branching ratio can be used to set a 95% confidence level upper limit of .74 on the branching fraction of the unobserved decay modes.

6. Summary

We have reported the results of a partial wave analysis of the $\bar{K}^0\pi^+\pi^-$ system produced at 11 *GeV/c*. The data sample has been obtained from a 1053 event/μb exposure of the LASS spectrometer, and consist of 7,636 events with $|t'| < 0.3$ $(GeV/c)^2$.

The natural spin-parity partial waves demonstrate the clear resonant behaviour

* The relative amounts of helicity 0 and helicity 1 production of both the D and G waves are consistent in the two channels.

of the leading 2^+ and 3^- waves. The K*(1430) and K*(1780) emerge as prominent structures in the partial wave decomposition. The 2^+ amplitudes provide new measurements of the mass, width, relative branching ratios and production characteristics of the K*(1430). The 3^- amplitudes demonstrate that the K*(1780) decays preferentially to $\mathrm{K}\pi$ and $\mathrm{K}^*(892)\pi$ rather than to $\mathrm{K}^*(1430)\pi$ or $\rho\mathrm{K}$.

The 4^+ intensity shows an enhancement around 2100 MeV/c^2 which is consistent with the K*(2060). There is also evidence for structure in the 2^+ intensity around 2000 MeV/c^2.

The $1^-0^-\rho P$ amplitude exhibits clear resonant behaviour around 1800 MeV/c^2, while there is evidence of resonant behaviour in the $1^-0^-\mathrm{K}^*P$ amplitude both at 1800 and 1400 MeV/c^2. The structure in the two waves at 1800 MeV/c^2 can be associated with the $\rho\mathrm{K}$ and $\mathrm{K}^*\pi$ decay modes of a single resonance, and the structure at 1400 MeV/c^2 in the $1^-0^-\mathrm{K}^*P$ wave can be interpreted as evidence for a second vector state[21].

The $1^+0^+\mathrm{K}^*S$ amplitude is quite strong in the 1300-1500 MeV/c^2 region and is consistent with it being due to the decay of the $Q_2(1400)$ along with a sizable background contribution. The $1^+0^+\epsilon S$ amplitude is the largest unnatural spin-parity wave in the higher mass region, but does not show any evidence of resonant structure. The lack of a second strong $\eta+$ amplitude in this region implies that the phases of the other $\eta+$ waves are too poorly measured to be of any value in understanding the $1^+0^+\epsilon S$ amplitude. The $2^-0^+\mathrm{K}^{**}S$ wave shows structure around 1750 MeV/c^2 which can be ascribed to the production and decay of the $L(1770)$ meson.

REFERENCES

1. C. Daum et al., Nucl. Phys. B187 (1981) 1.
2. G.W.Brandenburg et al., Phys. Rev. Lett. 36 (1976) 703.
3. Yu. Antipov et al., Nucl. Phys. B86 (1975) 365.
4. S. Tovey et al., Nucl. Phys. B95 (1975) 109.
5. G. Otter et al., Nucl. Phys. B93 (1975) 365.
6. M. Baubillier et al., Nucl. Phys. B202 (1982) 21.
7. A. Etkin et al., Phys. Rev. D22 (1980) 42.
8. E. Konigs et al., Phys. Lett. 74B (1978) 282.
9. J.S.M. Vergeest et al. Phys. Lett. 62B (1976) 471.
10. L. Bird et al. SLAC-PROPOSAL-E-132, (1976).
11. D. Aston et al. Phys. Lett. 99B (1981) 503.
12. A. Honma, SLAC-0235, (1980) Ph.D. Thesis.
13. D. Aston et al. Phys. Lett. 106B (1981) 235.
14. P.F.Kunz et al., IEEE Trans. NS27 (1980) 582.
15. D. Aston et al., report in preparation.
16. J.D. Hansen et al., Nucl. Phys. B81 (1974) 403.
17. P. Estabrooks et al., Nucl. Phys. B133 (1978) 490.
18. M. Roos., Nucl. Phys. B97 (1975) 165.
19. P. Estabrooks et al., Nucl. Phys. B95 (1975) 322.
20. W.E. Cleland et al. Phys. Lett. 97B (1980) 465.
21. D. Aston et al., SLAC-PUB-3315 (1984).
22. J. D. Jackson, Nuovo Cim. 34 (1964) 1144.
23. Particle Data Group; C. G. Wohl et al., Rev.Mod.Phys. 56 (1984).

TABLE CAPTIONS

1. The mass binning used in the partial wave analysis.
2. The t' binning used in the partial wave analysis. The number of events in each t' bin is shown for the two $\bar{K}^0\pi^+\pi^-$ mass regions 1350-1510 MeV/c^2 and 1710-1890 MeV/c^2.
3. The slope parameter values for the dominant waves in the 1350-1510 and 1710-1890 MeV/c^2 mass bins. The parameters in the low mass bin are for the Branch I solutions.
4. The measured branching ratio values for the K*(1430) and K*(1780).

TABLE 1

Bin Center (MeV/c^2)	Bin Width (MeV/c^2)	Events
1160	140	210
1210	120	234
1280	100	346
1320	100	473
1370	80	558
1410	80	758
1450	80	830
1490	80	757
1530	80	636
1570	80	554
1610	80	552
1650	80	557
1700	100	763
1740	100	831
1800	100	866
1840	100	848
1900	100	749
1950	120	854
2010	120	810
2070	120	755
2130	120	715
2210	160	867

TABLE 2

Bin Center $(GeV/c)^2$	Bin Width $(GeV/c)^2$	Events	
		1350-1510 MeV/c^2	1710-1890 MeV/c^2
0.050	0.100	762	862
0.200	0.200	685	652
0.450	0.300	422	373
0.800	0.400	214	191

TABLE 3

Wave	Slope $(GeV/c)^{-2}$	
	1350-1510 MeV/c^2	1710-1890 MeV/c^2
1^+0^+ K$^*S$	-3.2 ± 0.5	
1^-0^- K$^*P$	-2.1 ± 0.4	-5.6 ± 0.7
$1^-0^-\rho P$		-8.2 ± 0.9
2^+0^- K$^*D$	-11.5 ± 2.0	
$2^+0^-\rho D$	-8.9 ± 2.1	
3^-0^- K$^*F$		-11.8 ± 3.7

TABLE 4

	K*(1430)	K*(1780)
BR(K$^*\pi$/Kπ)	$0.44 \pm .09$	$1.09 \pm .26$
BR(ρK/Kπ)	$0.18 \pm .05$	
BR(ρK/K$^*\pi$)	$0.42 \pm .08$	$<.77$ (95% c.l.)
BR(K$^{**}\pi$/K$^*\pi$)		<1.78 (95% c.l.)

FIGURE CAPTIONS

1. The plan view of the LASS spectrometer.
2. The invariant mass distribution of the V^0 sample assuming a $p\pi^-$ decay. The shaded region indicates events removed as Λ^0's.
3. The invariant mass distribution of the final V^0 decay sample assuming a $\pi^+\pi^-$ decay.
4. The K^+K^- invariant mass distribution of the two charged prongs seen at the primary vertex before (all events) and after (unshaded events) the ϕ cut.
5. The missing mass squared against the $\bar{K}^0\pi^+\pi^-$ system. The events in the unshaded region were used in the PWA.
6. The missing mass squared recoiling against the $\bar{K}^0\pi^-$ system; the shaded events are removed by applying the "Δ" and "$\bar{K}^0\pi^- p\,\pi^0$" cuts (see text).
7. Missing mass squared against the $\bar{K}^0\pi^- p$ system. The shaded events are removed by applying the "Δ" and "$\bar{K}^0\pi^- p\,\pi^0$" cuts.
8. The $\bar{K}^0\pi^+\pi^-$ invariant mass distribution for the data sample used for the isobar analysis ($|t'| < 0.3\ (GeV/c)^2$).
9. The Dalitz plot for the $\bar{K}^0\pi^+\pi^-$ event sample. The curves show the physical region for $M(\bar{K}^0\pi^+\pi^-) = 1010$ and 2300 MeV/c^2, the low and high mass limits of the data used for the PWA.
10. The Dalitz plot for events with $M(\bar{K}^0\pi^+\pi^-) \leq 1550\ MeV/c^2$. The curves show the physical boundaries for $M(\bar{K}^0\pi^+\pi^-) = 1010$ and 1550 MeV/c^2.
11. The Dalitz plot for events with $1550 < M(\bar{K}^0\pi^+\pi^-) \leq 1950\ MeV/c^2$. The curves show the physical boundaries for $M(\bar{K}^0\pi^+\pi^-) = 1550$ and 1950 MeV/c^2.
12. The Dalitz plot for events with $M(\bar{K}^0\pi^+\pi^-) > 1950\ MeV/c^2$. The curves show the physical boundaries for $M(\bar{K}^0\pi^+\pi^-) = 1950$ and 2300 MeV/c^2.
13. A schematic representation of the isobar model description for the production of the 3-meson final state.
14. The final wave set used in the analysis.

15. The natural parity J^P sums for the partial waves in this analysis.

16. The unnatural parity J^P sums for the partial waves in this analysis.

17. The $1^-0^-\,\mathrm{K}^*P$ and $1^-0^-\rho P$ intensities and relative phases for $|t'| < 0.3\ (GeV/c)^2$. Branch I solutions are shown as solid points and Branch II solutions are shown as open circles. The phases are measured relative to the $1^-0^-\,\mathrm{K}^*P$ wave (see text).

18. The intensities and relative phases of the $2^+0^-\,\mathrm{K}^*D$ and $2^+0^-\rho D$ waves for $|t'| < 0.3\ (GeV/c)^2$. Branch I solutions are shown as solid points and Branch II solutions are shown as open circles. The phases are measured relative to the $1^-0^-\,\mathrm{K}^*P$ wave. The curves are from the fit described in the text.

19. The intensities and relative phases of the $2^+1^+\,\mathrm{K}^*D$ and $2^+1^-\,\mathrm{K}^*D$ waves for $|t'| < 0.3\ (GeV/c)^2$. The $2^+1^+\,\mathrm{K}^*D$ phase is measured relative to the $1^+0^+\,\mathrm{K}^*S$ wave. The $2^+1^-\,\mathrm{K}^*D$ wave is too small to provide a reliable phase measurement. The curve on the intensity of the $2^+1^+\,\mathrm{K}^*D$ wave is from the fit described in the text.

20. The intensities and relative phases of the 3^- partial waves for $|t'| < 0.3\ (GeV/c)^2$. The phases are measured relative to the $1^-0^-\,\mathrm{K}^*P$ wave. The curve on the $3^-0^-\,\mathrm{K}^*F$ intensity is from the fit described in the text.

21. The $0^-0^+\epsilon S$, $2^-0^+\,\mathrm{K}^{**}S$ and $2^-0^+ f S$ intensities and relative phases for $|t'| < 0.3\ GeV/c^2$. The phases are measured relative to the $1^+0^+\,\mathrm{K}^*S$ up to 1650 MeV/c^2 and relative to the $1^+0^+\epsilon S$ above that mass. The $2^-0^+ f S$ wave is too small to provide a reliable phase measurement.

22. The $1^+0^+\,\mathrm{K}^*S$, $1^+0^+\rho S$ and $1^+0^+\epsilon S$ intensities and relative phases for $|t'| < 0.3 GeV/c^2$. The phases are measured relative to the $1^+0^+\,\mathrm{K}^*S$ up to 1650 MeV/c^2 and relative to the $1^+0^+\epsilon S$ above that mass. For small wave intensities, the phase is unmeasurable.

23. The t' dependences of the largest waves in two mass bins; 1350-1510 MeV/c^2(solid points and lines) and 1710-1890 MeV/c^2(open points and dashed lines). The solid triangles indicate Branch II solutions while the solid points indicate Branch I solutions. The lines represent the exponential fits described in the text.

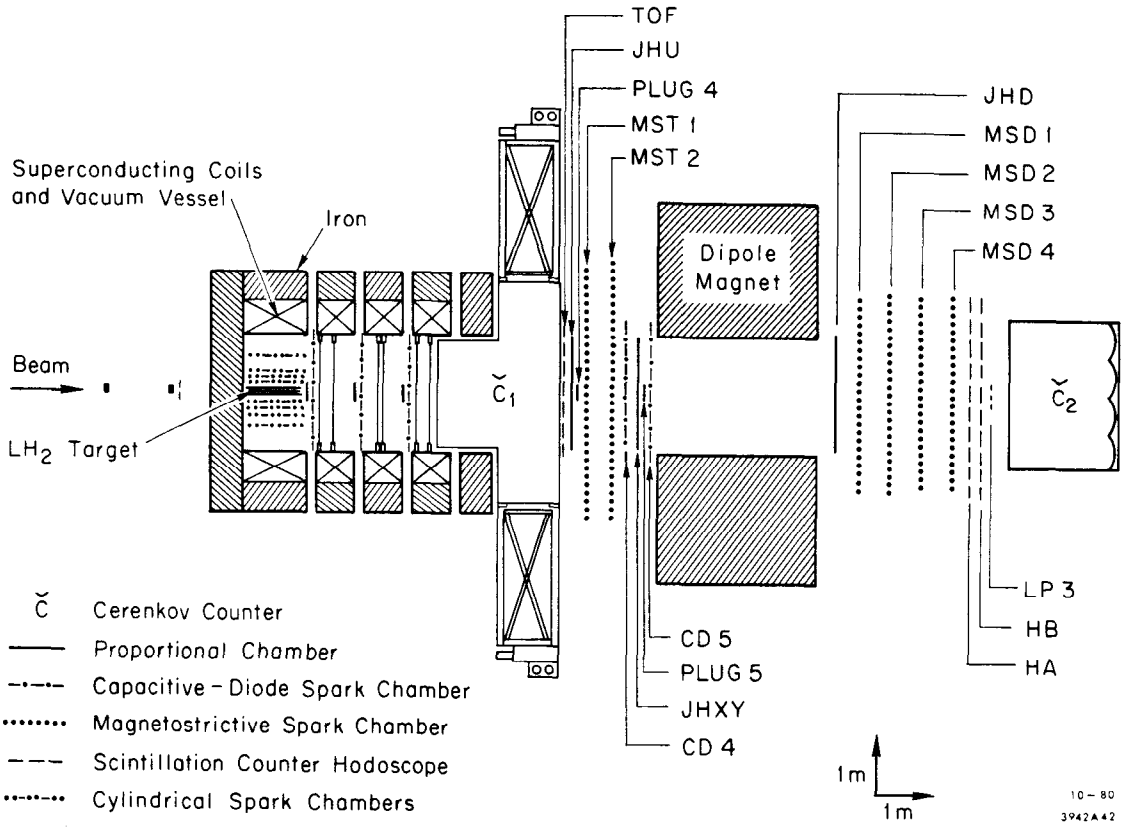
TOF
JHU
PLUG 4
MST 1
MST 2
JHD
MSD 1
MSD 2
MSD 3
MSD 4
Superconducting Coils
and Vacuum Vessel
Iron
Dipole
Magnet
Beam
LH_2 Target
$\check{C}_1$
$\check{C}_2$
LP 3
HB
HA
CD 5
PLUG 5
JHXY
CD 4
$\check{C}$ Cerenkov Counter
Proportional Chamber
Capacitive - Diode Spark Chamber
Magnetostrictive Spark Chamber
Scintillation Counter Hodoscope
Cylindrical Spark Chambers
1m
1m
10-80
3942A42

Fig. 1

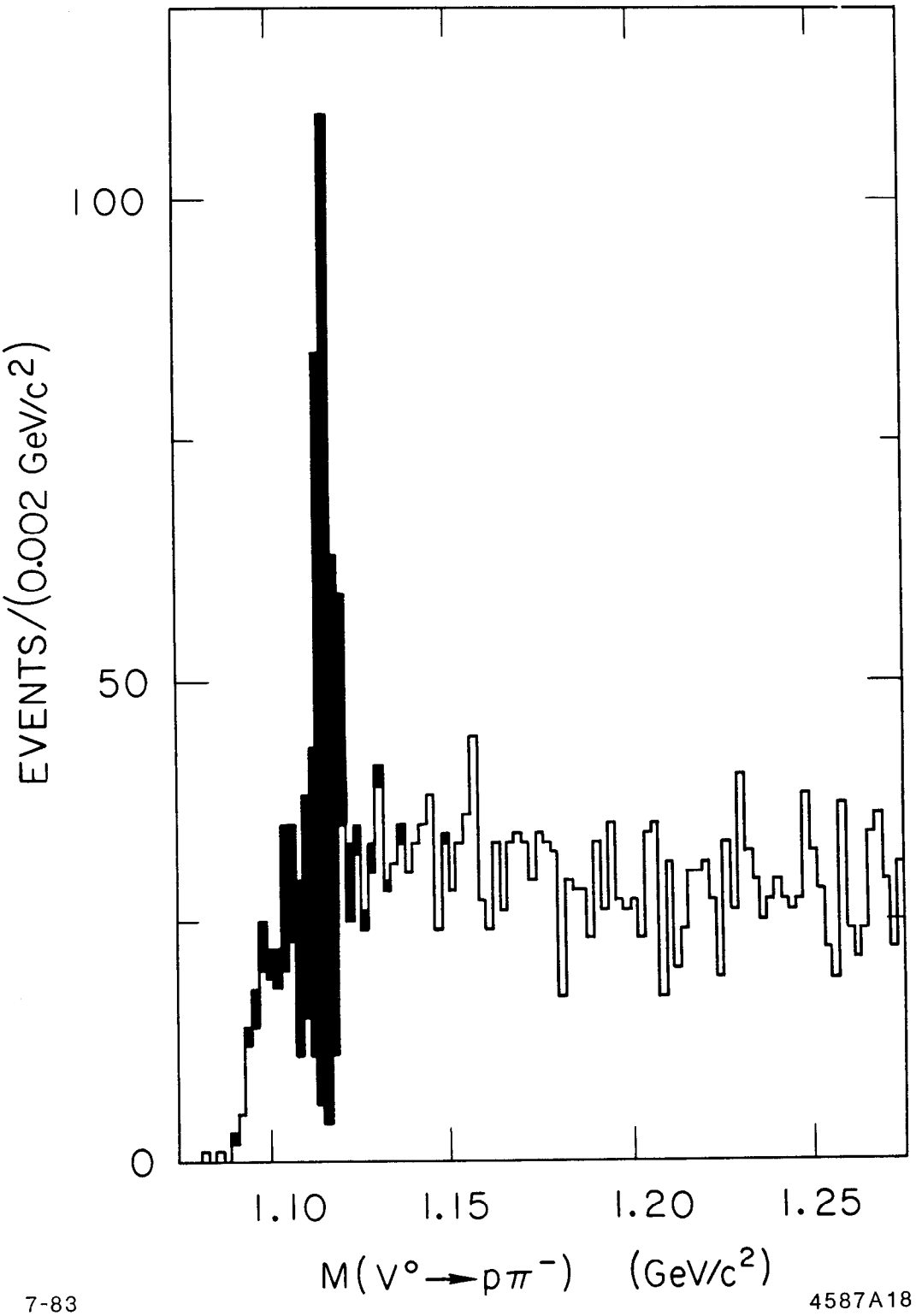
100
50
0
EVENTS/(0.002 GeV/c²)
1.10
1.15
1.20
1.25
M(V°→pπ⁻) (GeV/c²)
7-83
4587A18

Fig 2

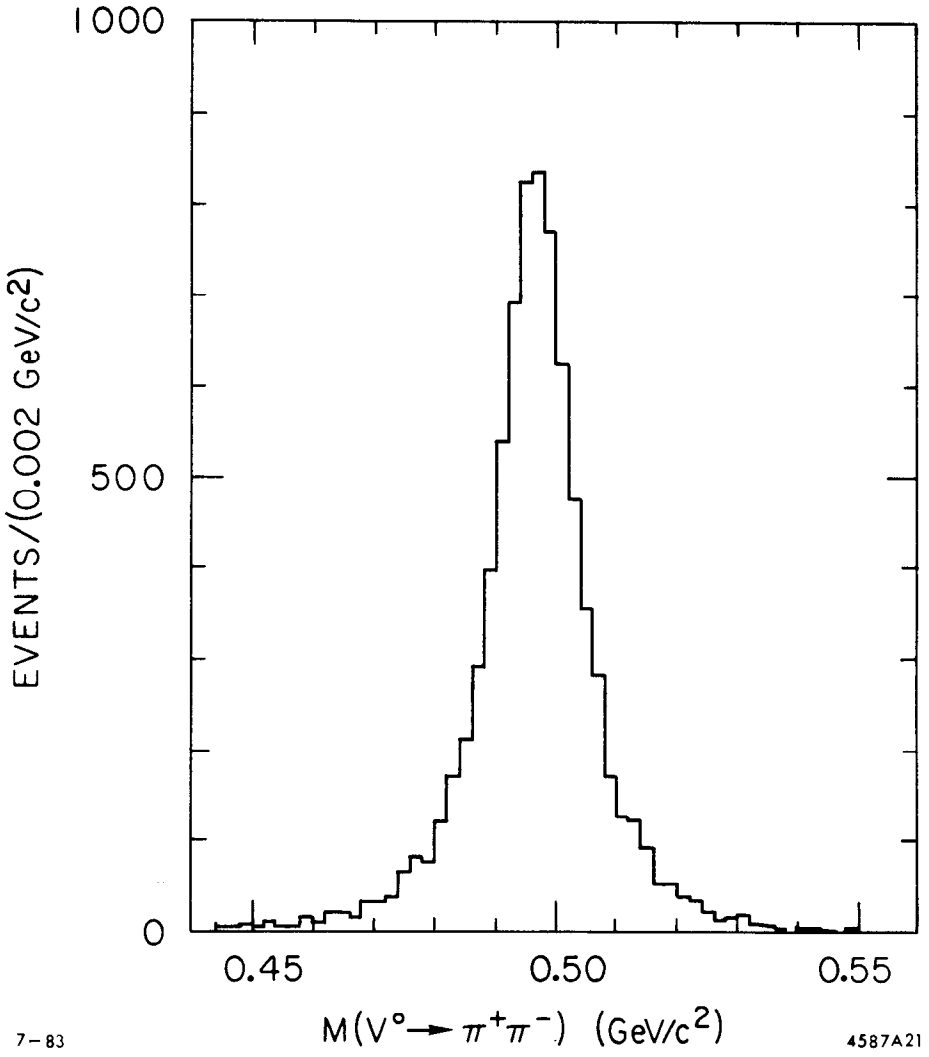
1000
500
0
EVENTS/(0.002 GeV/c²)
0.45
0.50
0.55
M(V°→ π⁺π⁻) (GeV/c²)
7-83
4587A21

Fig. 3

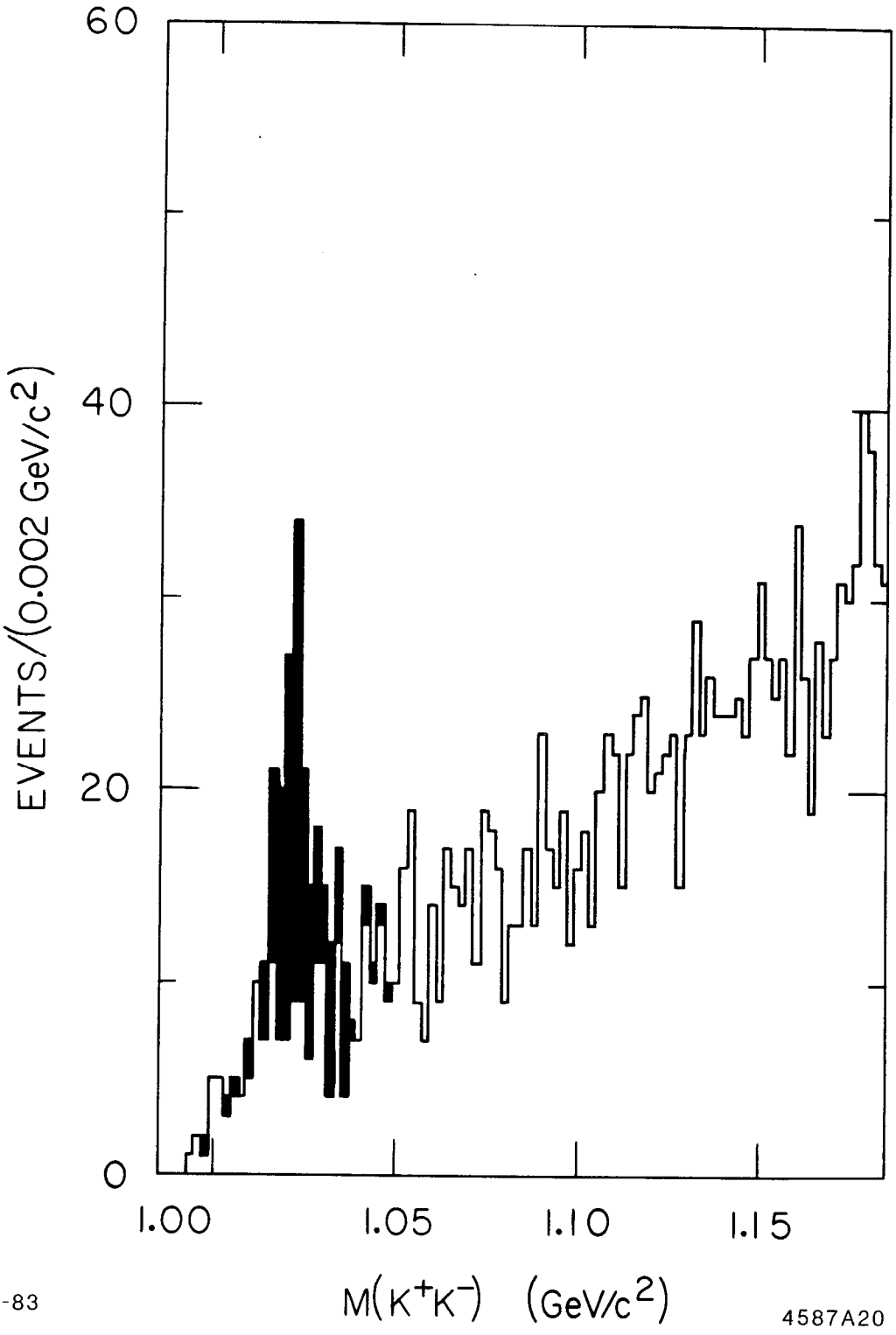
60
40
20
0
EVENTS/(0.002 GeV/c²)
1.00
1.05
1.10
1.15
M(K⁺K⁻) (GeV/c²)
7-83
4587A20

Fig. 4

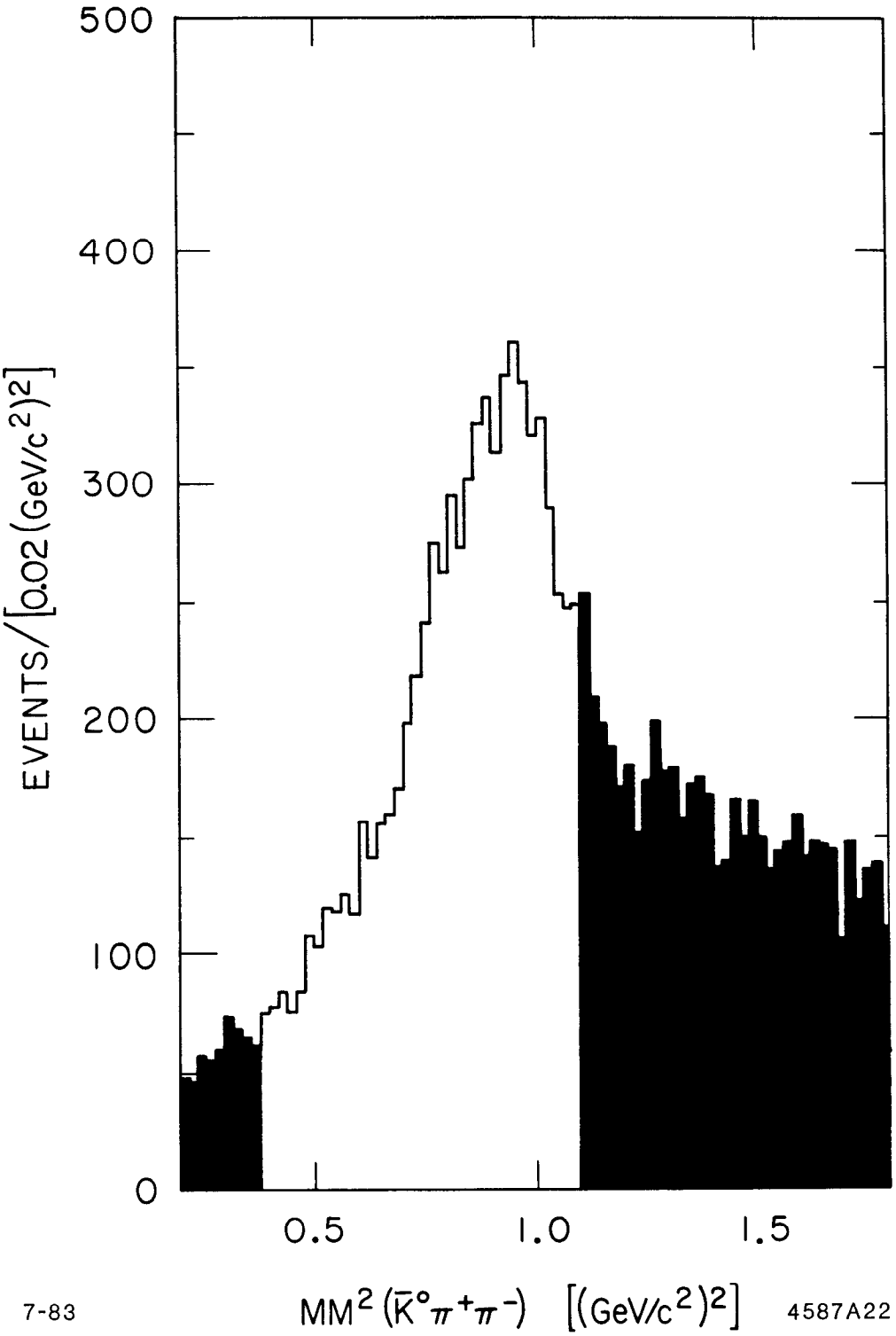
500
400
300
200
100
0
EVENTS/[0.02(GeV/c²)²]
0.5
1.0
1.5
MM²(K°π⁺π⁻) [(GeV/c²)²]
7-83
4587A22

Fig. 5

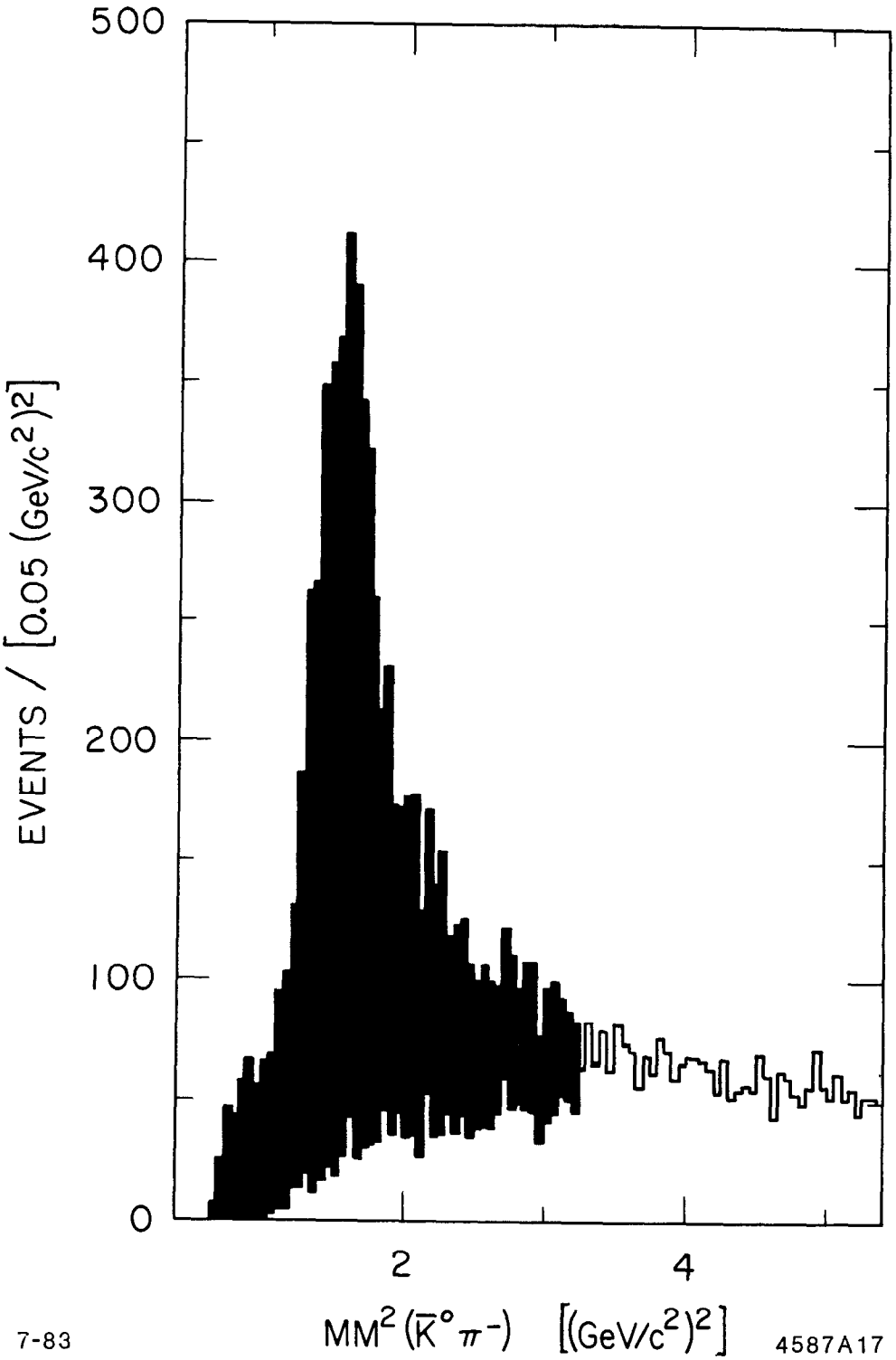
500
400
300
200
100
0
EVENTS / [0.05 (GeV/c²)²]
2
4
MM² (K̄°π⁻) [(GeV/c²)²]
7-83
4587A17

Fig 6

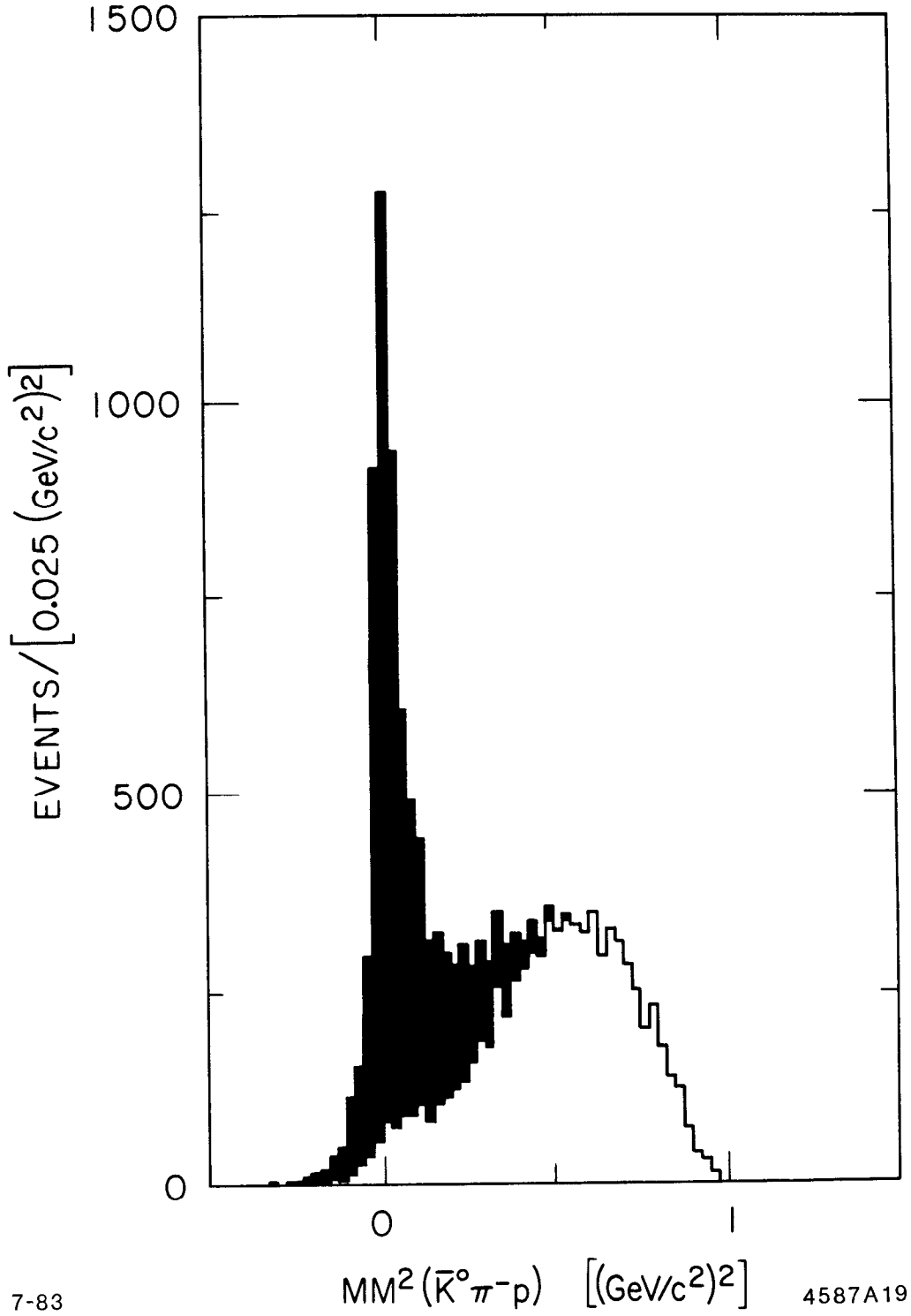
1500
1000
500
0
EVENTS/[0.025 (GeV/c²)²]
0
1
MM² (K̄°π⁻p) [(GeV/c²)²]
7-83
4587A19

Fig. 7

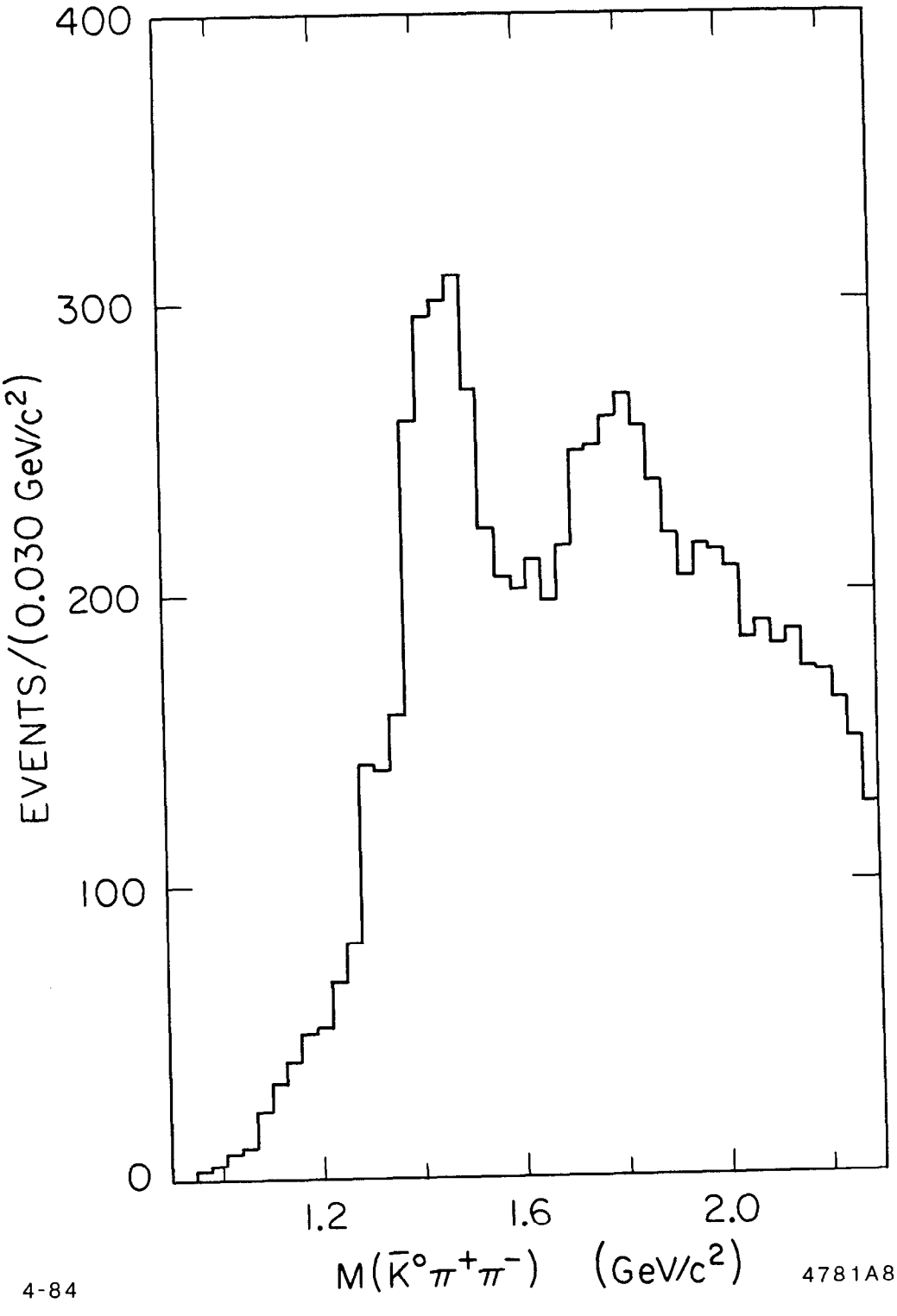
400
300
200
100
0
EVENTS/(0.030 GeV/c²)
1.2
1.6
2.0
M(K̄°π⁺π⁻) (GeV/c²)
4-84
4781A8

Fig. 8

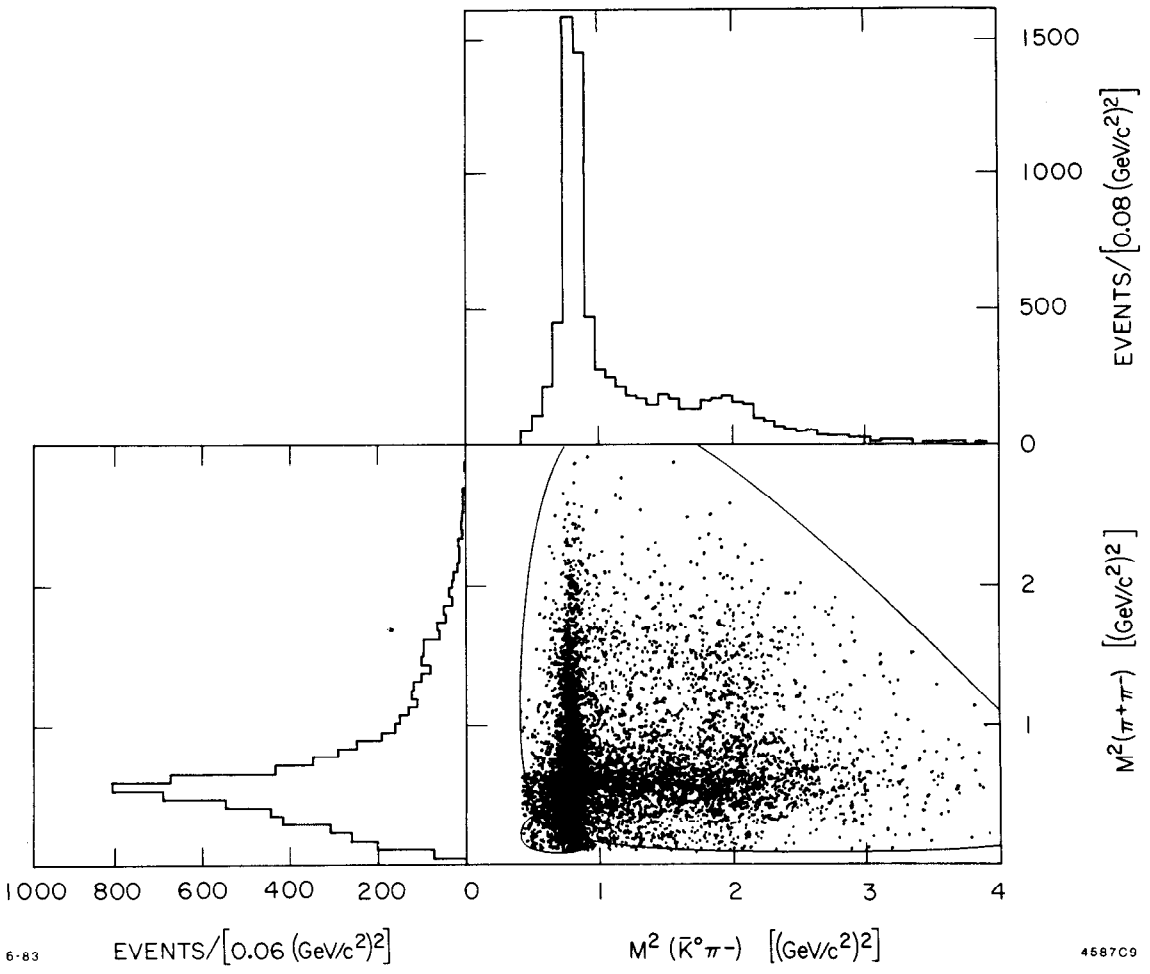
1500
1000
500
0
EVENTS/[0.08 (GeV/c²)²]
2
1
M²(π⁺π⁻) [(GeV/c²)²]
1000 800 600 400 200 0
EVENTS/[0.06 (GeV/c²)²]
1 2 3 4
M² (K°π⁻) [(GeV/c²)²]
6-83
4587C9

Fig. 9

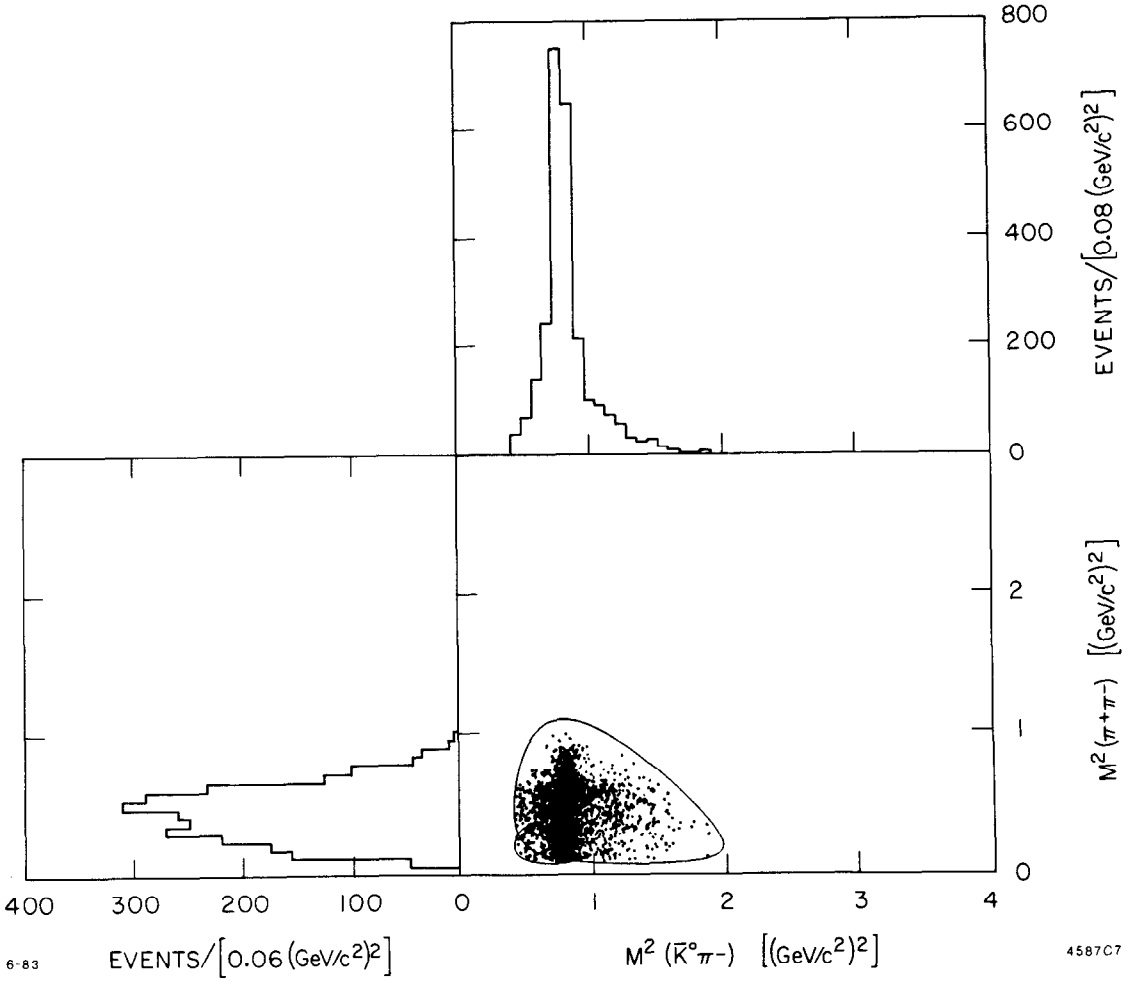
800
600
400
200
0
EVENTS/[0.08 (GeV/c²)²]
2
1
0
M²(π⁺π⁻) [(GeV/c²)²]
400
300
200
100
0
1
2
3
4
6-83
EVENTS/[0.06 (GeV/c²)²]
M² (K°π⁻) [(GeV/c²)²]
4587C7

Fig. 10

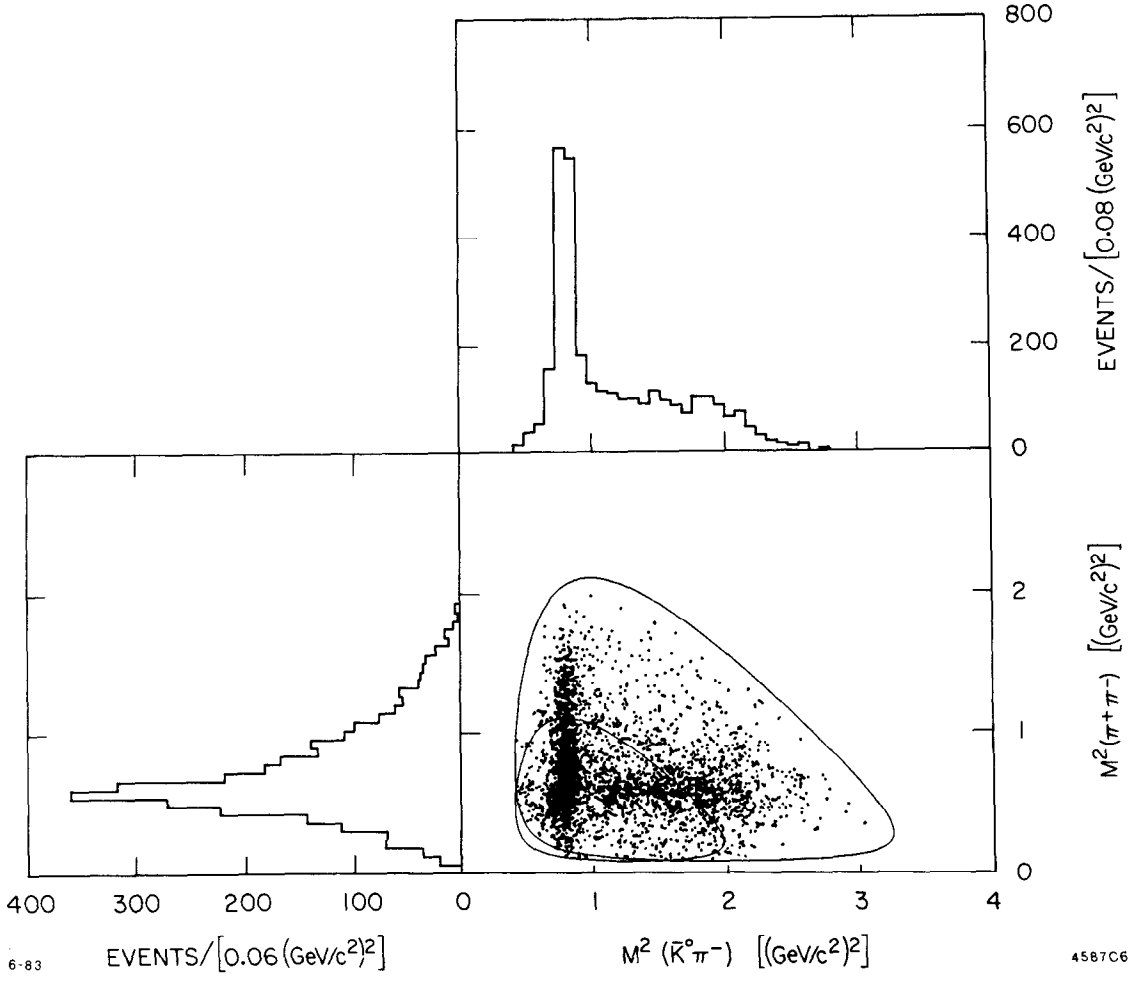
800
600
400
200
0
EVENTS/[0.08 (GeV/c²)²]
2
1
0
M²(π⁺π⁻) [(GeV/c²)²]
400
300
200
100
0
1
2
3
4
6-83
EVENTS/[0.06 (GeV/c²)²]
M² (K°π⁻) [(GeV/c²)²]
4587C6

Fig. 11

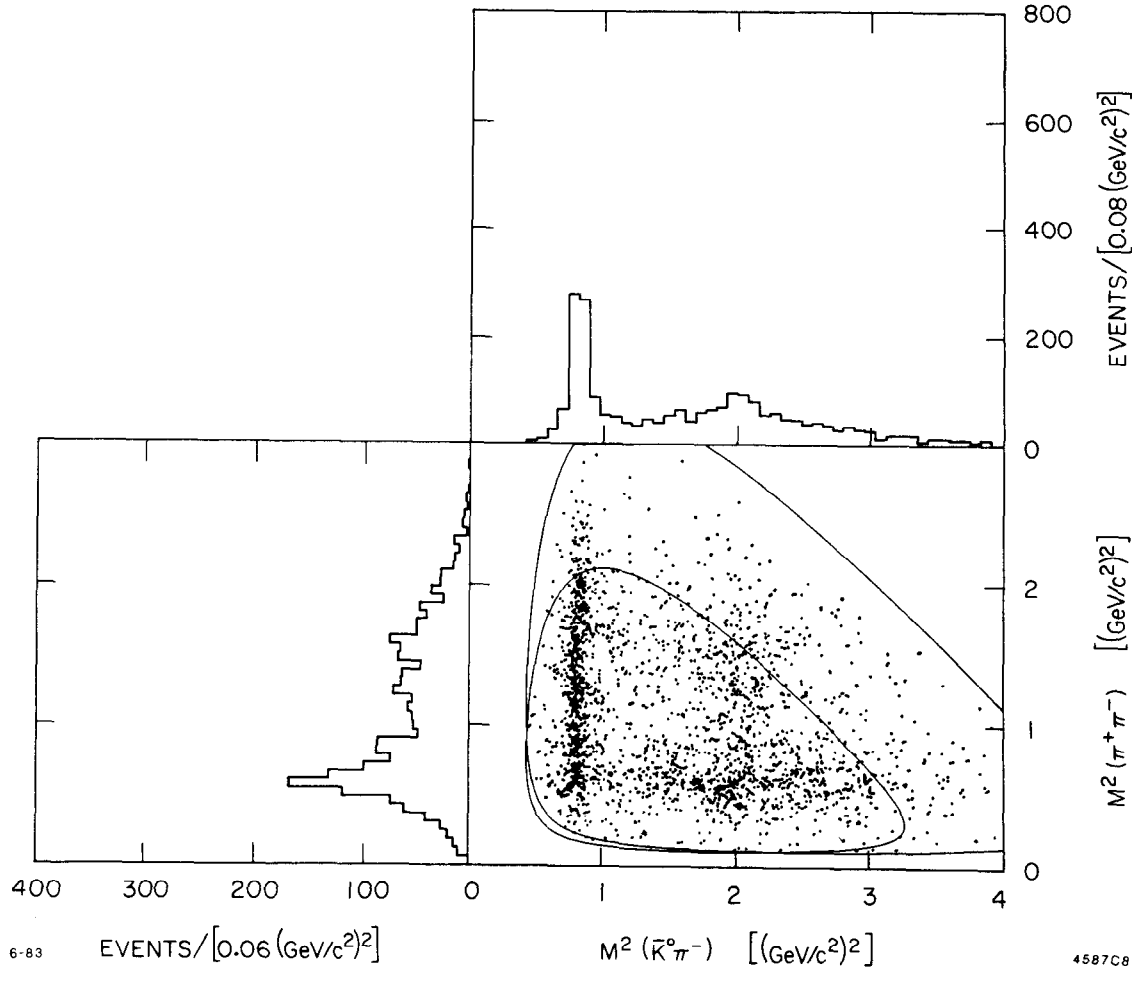
800
600
400
200
0
EVENTS/[0.08 (GeV/c²)²]
2
1
0
M² (π⁺π⁻) [(GeV/c²)²]
400
300
200
100
0
1
2
3
4
6-83
EVENTS/[0.06 (GeV/c²)²]
M² (K̄°π⁻) [(GeV/c²)²]
4587C8

Fig. 12

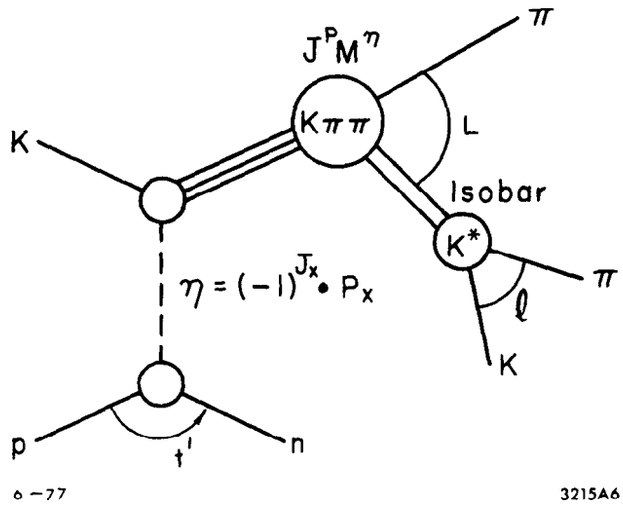
$J^P M^\eta$
π
$K\pi\pi$
L
K
Isobar
K^*
$\eta = (-1)^{J_x} \cdot P_x$
π
ℓ
K
p
n
t'
6-77
3215A6

Fig. 13

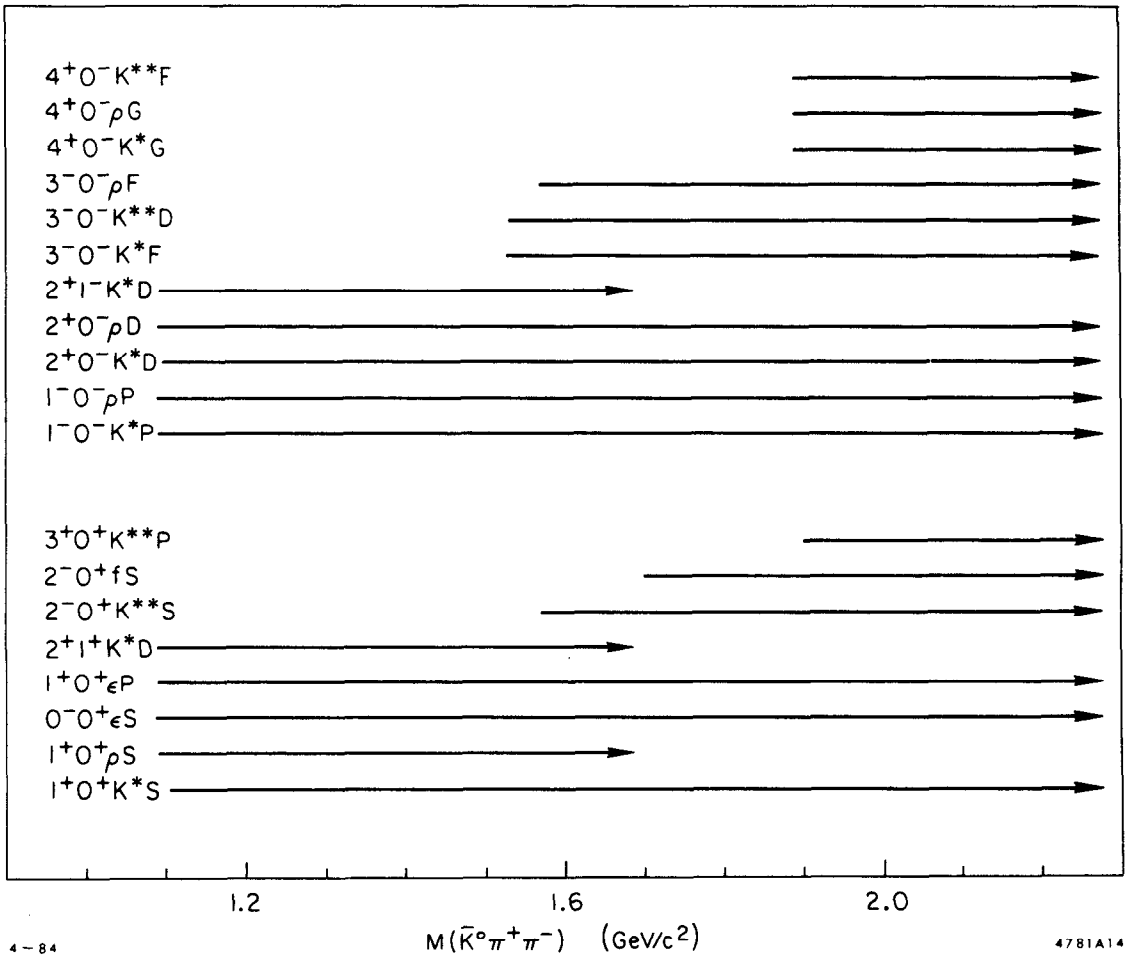
$4^+0^-K^{**}F$
$4^+0^-\rho G$
$4^+0^-K^*G$
$3^-0^-\rho F$
$3^-0^-K^{**}D$
$3^-0^-K^*F$
$2^+1^-K^*D$
$2^+0^-\rho D$
$2^+0^-K^*D$
$1^-0^-\rho P$
$1^-0^-K^*P$
$3^+0^+K^{**}P$
2^-0^+fS
$2^-0^+K^{**}S$
$2^+1^+K^*D$
$1^+0^+\epsilon P$
$0^-0^+\epsilon S$
$1^+0^+\rho S$
$1^+0^+K^*S$
1.2
1.6
2.0
$M(\bar{K}^0\pi^+\pi^-)$ (GeV/c^2)
4-84
4781A14

Fig. 14

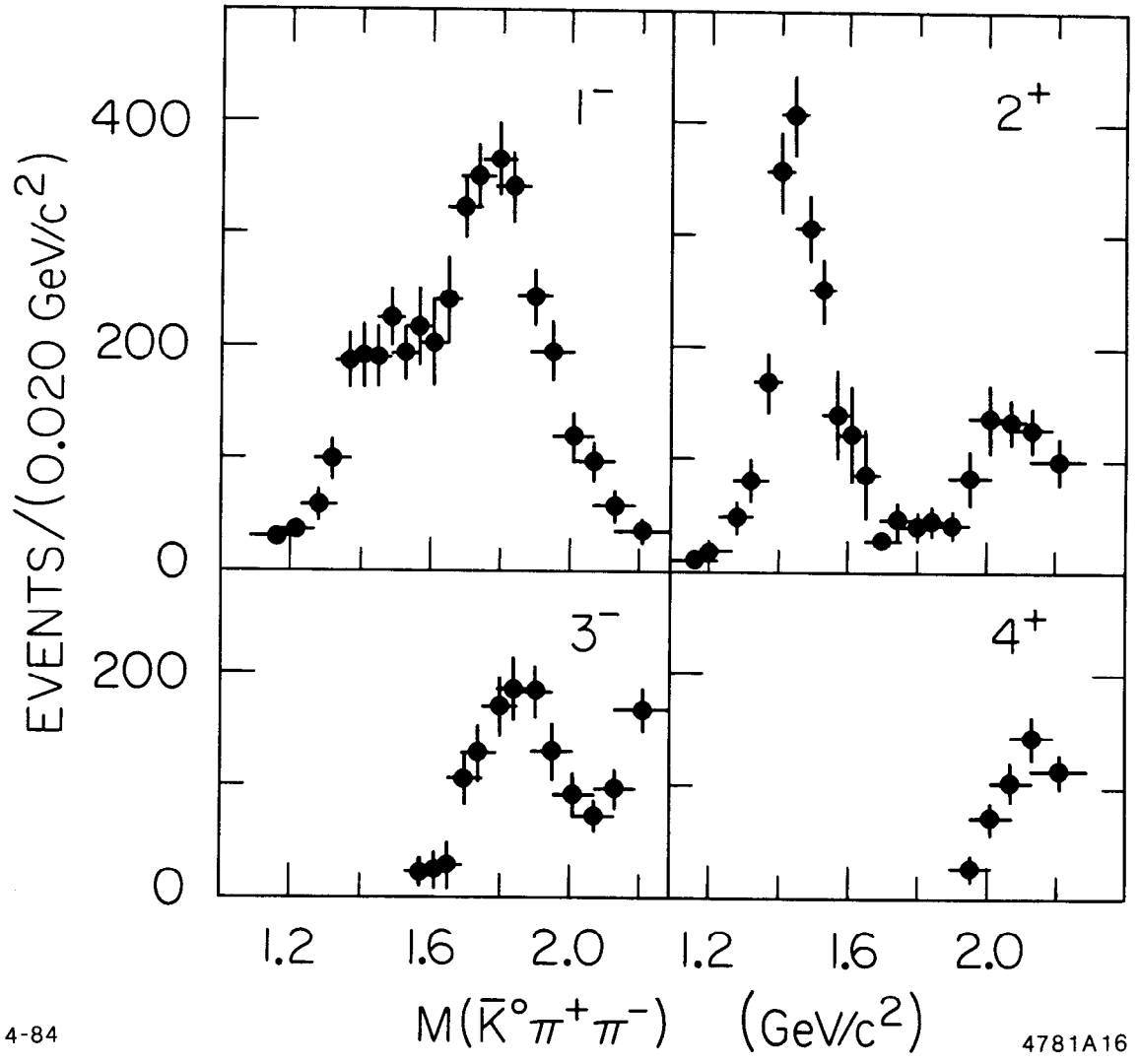
400
200
0
200
0
EVENTS/(0.020 GeV/c²)
1⁻
2⁺
3⁻
4⁺
1.2
1.6
2.0
1.2
1.6
2.0
M(K̄°π⁺π⁻) (GeV/c²)
4-84
4781A16

Fig. 15

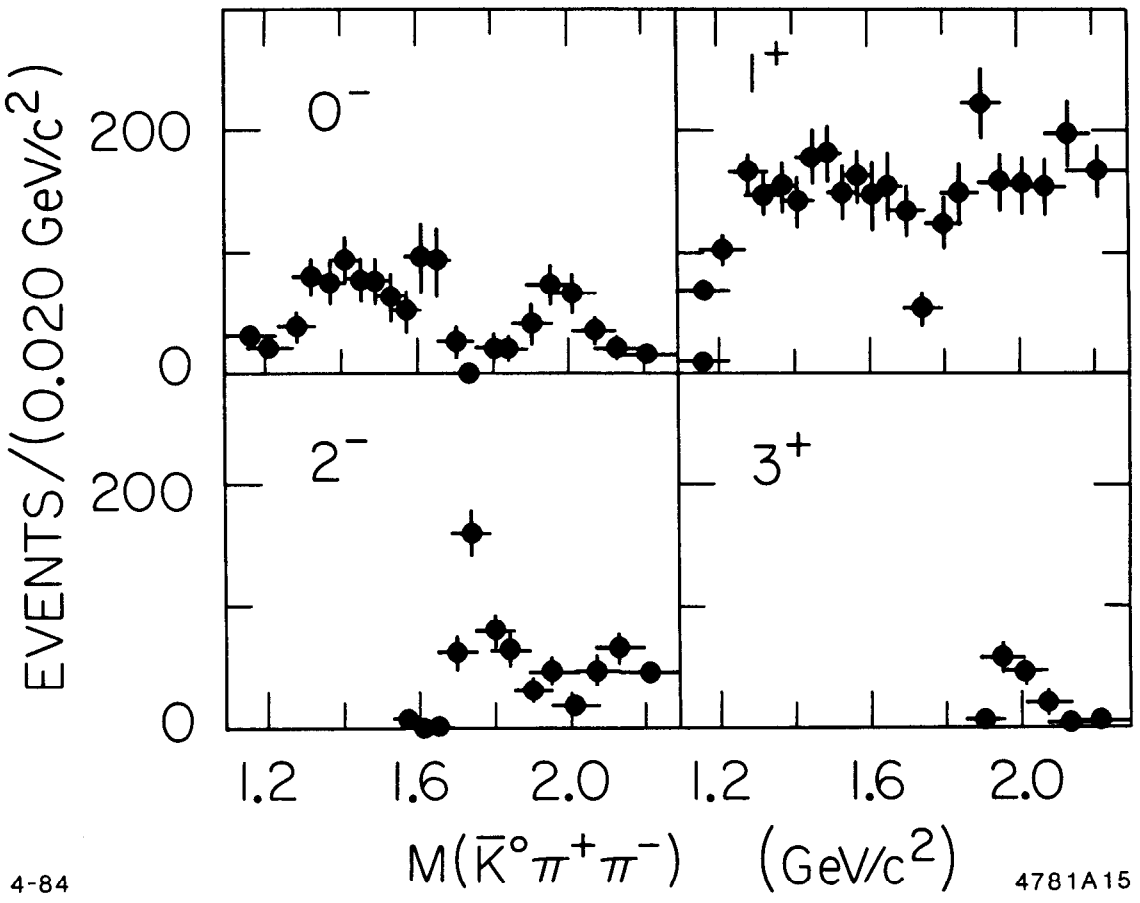
0⁻
1⁺
2⁻
3⁺
200
0
200
0
EVENTS/(0.020 GeV/c²)
1.2
1.6
2.0
1.2
1.6
2.0
M(K̄°π⁺π⁻) (GeV/c²)
4-84
4781A15

Fig. 16

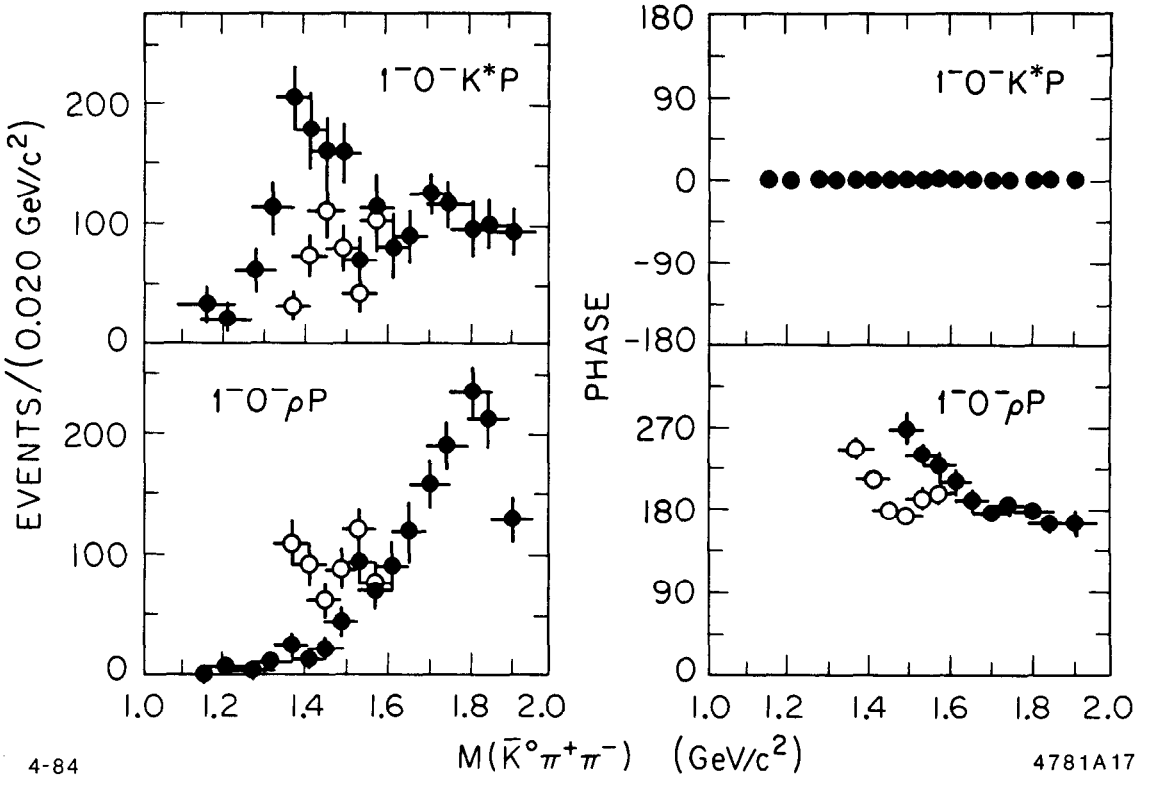
EVENTS/(0.020 GeV/c²)
1⁻0⁻K*P
1⁻0⁻ρP
200
100
0
1.0
1.2
1.4
1.6
1.8
2.0
M(K̄°π⁺π⁻)
PHASE
180
90
0
-90
-180
270
(GeV/c²)
4-84
4781A17

Fig. 17

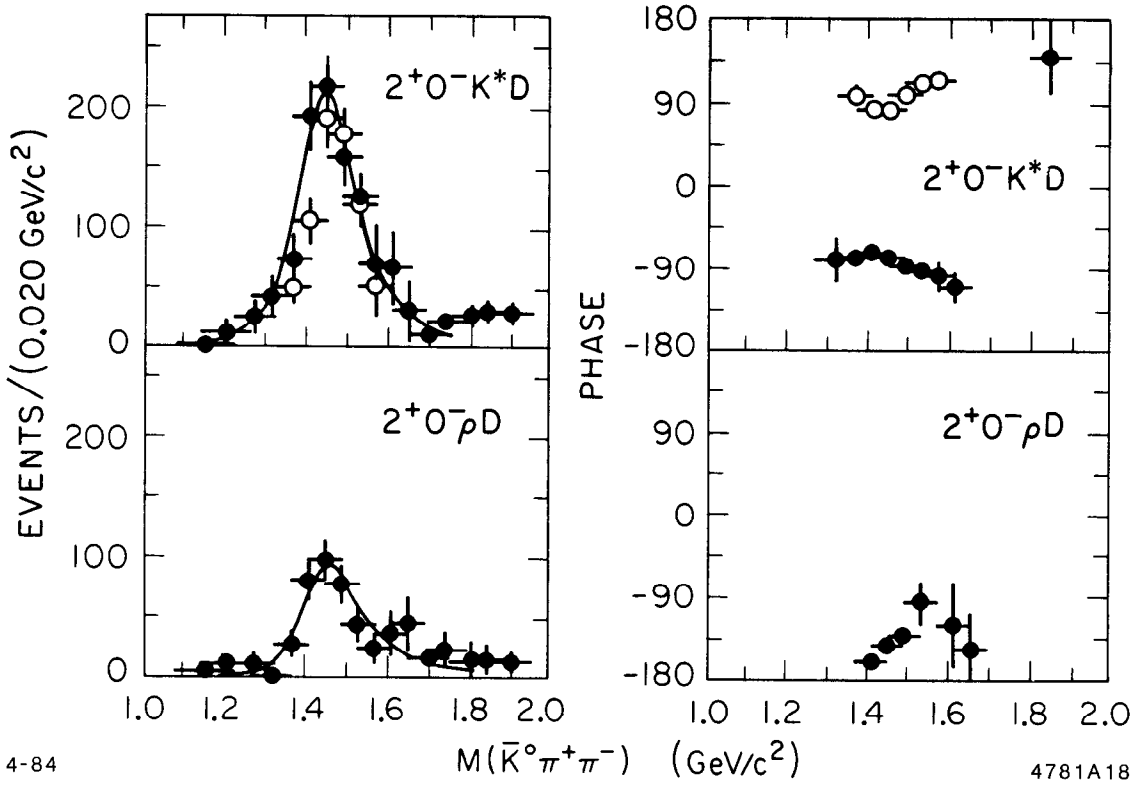
EVENTS/(0.020 GeV/c²)
2⁺0⁻K*D
2⁺0⁻ρD
200
100
0
PHASE
180
90
-90
-180
1.0
1.2
1.4
1.6
1.8
2.0
M(K̄°π⁺π⁻) (GeV/c²)
4-84
4781A18

Fig. 18

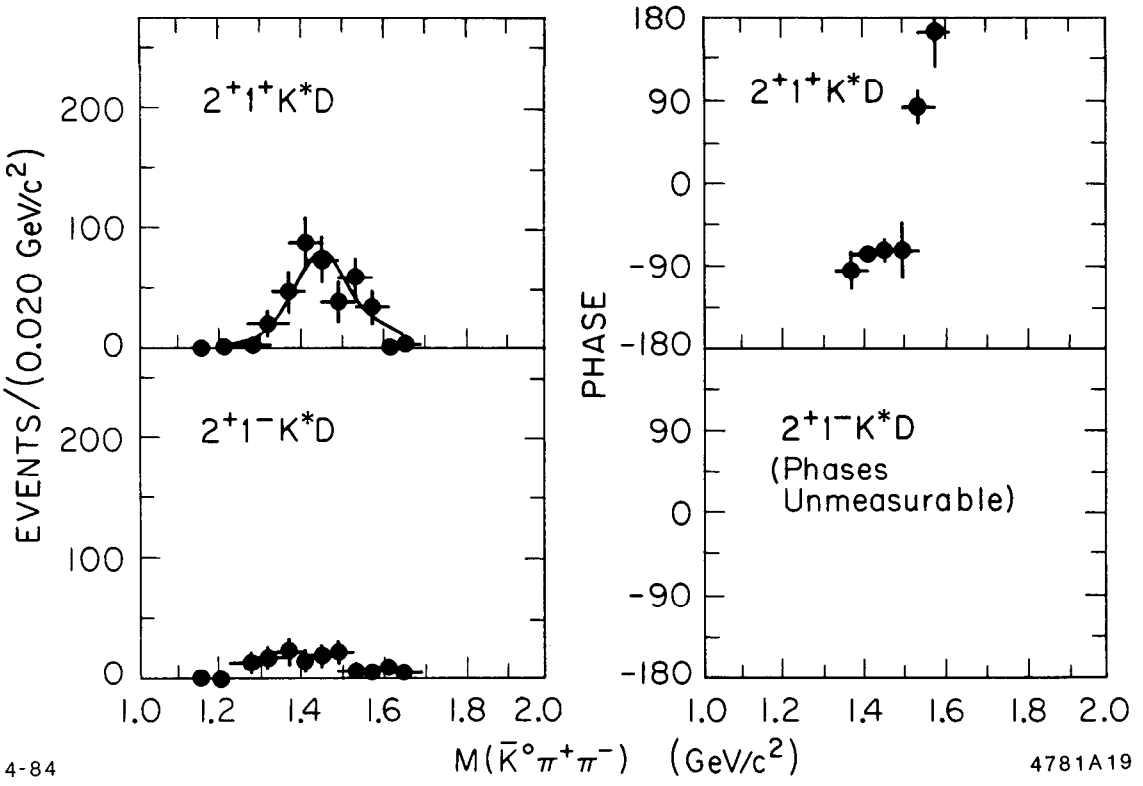
EVENTS/(0.020 GeV/c²)
2⁺1⁺K*D
2⁺1⁻K*D
200
100
0
200
100
0
1.0
1.2
1.4
1.6
1.8
2.0
M(K̄°π⁺π⁻) (GeV/c²)
PHASE
180
90
0
-90
-180
90
0
-90
-180
(Phases
Unmeasurable)
4-84
4781A19

Fig. 19

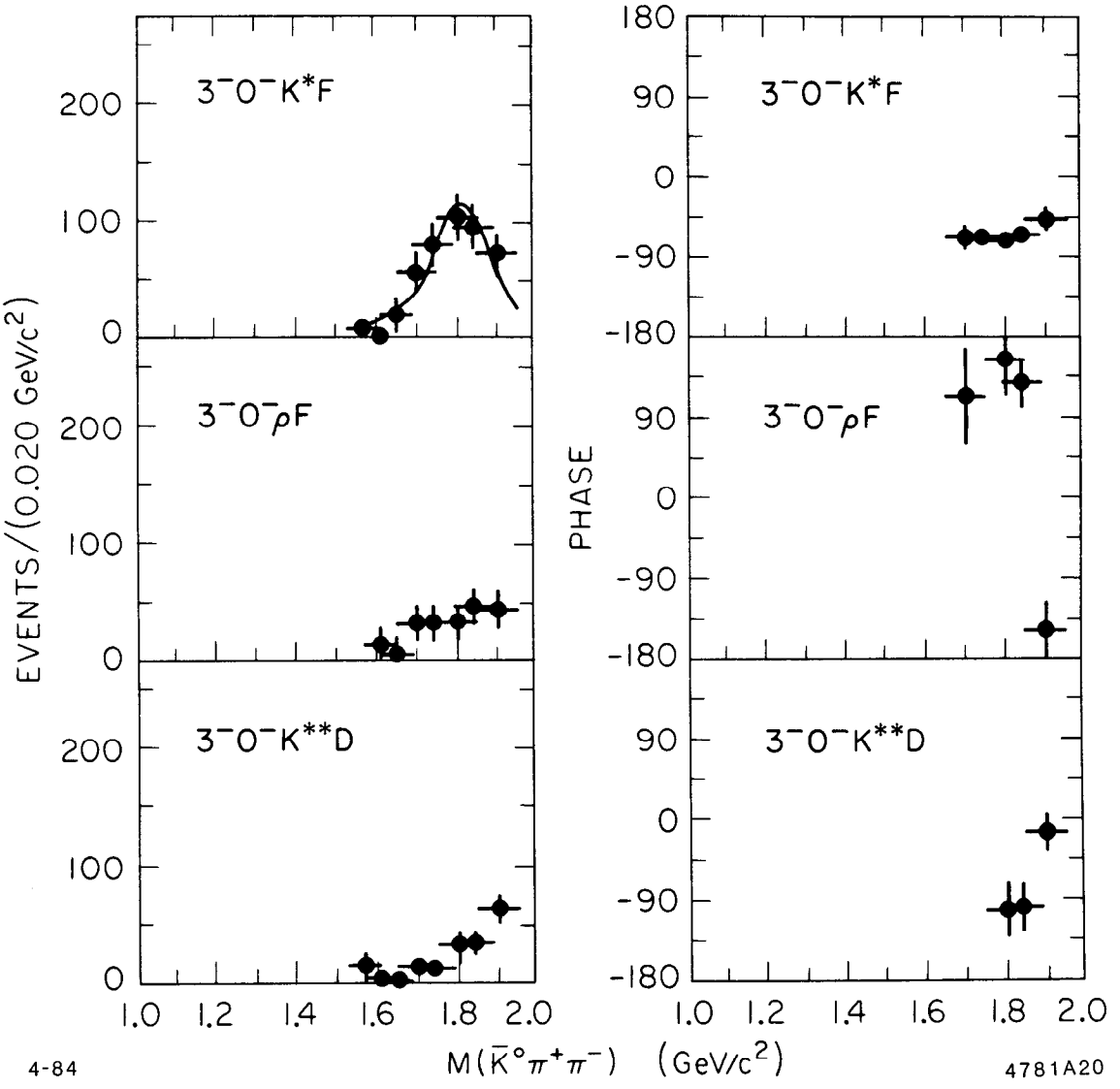
3⁻0⁻K*F
3⁻0⁻ρF
3⁻0⁻K**D
EVENTS/(0.020 GeV/c²)
PHASE
M(K̄°π⁺π⁻) (GeV/c²)
4-84
4781A20

Fig. 20

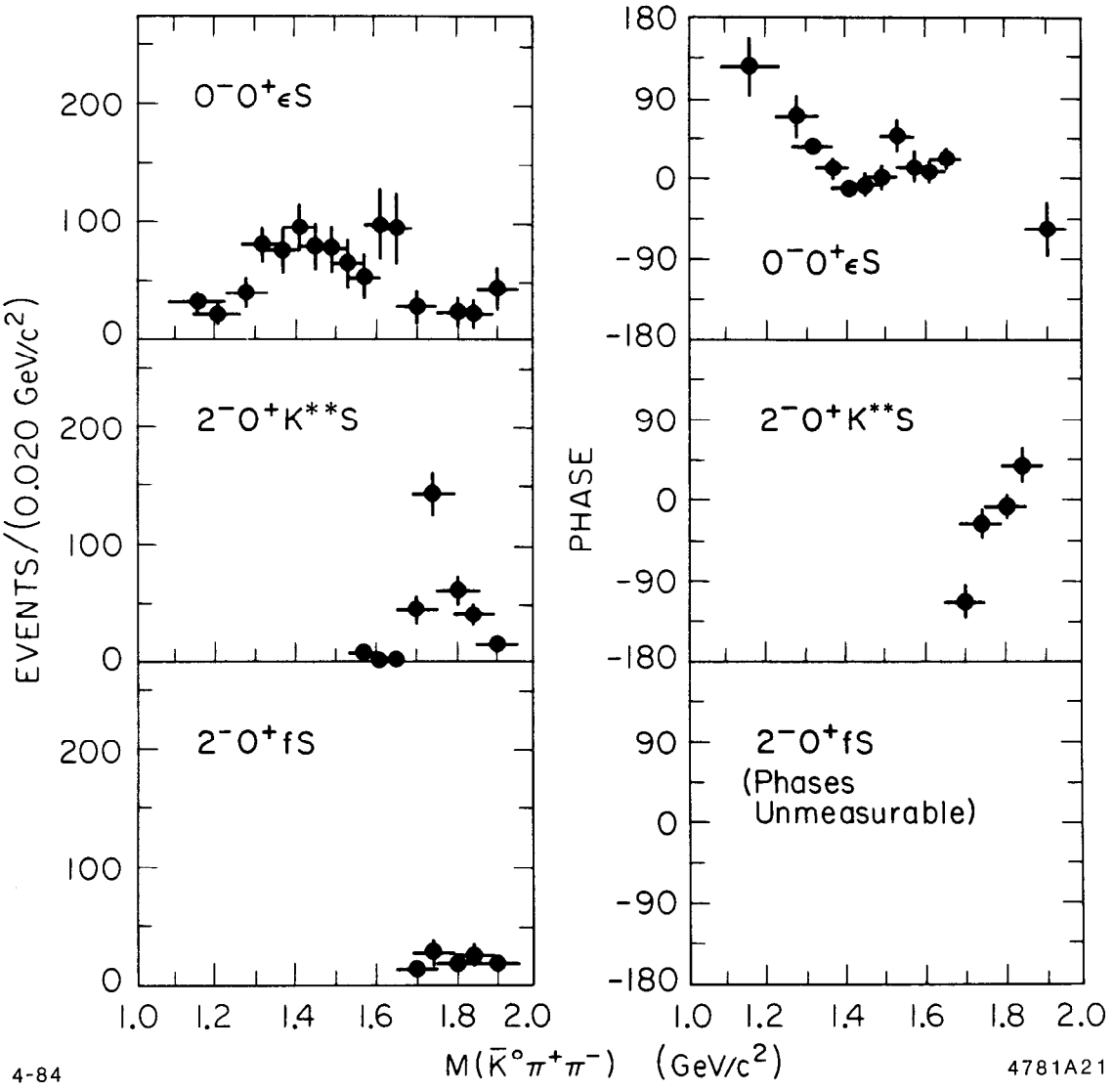
$0^-0^+\epsilon S$
$2^-0^+K^{**}S$
2^-0^+fS
(Phases Unmeasurable)
EVENTS/(0.020 GeV/c²)
PHASE
M($\bar{K}^0\pi^+\pi^-$) (GeV/c²)
4-84
4781A21

Fig. 21

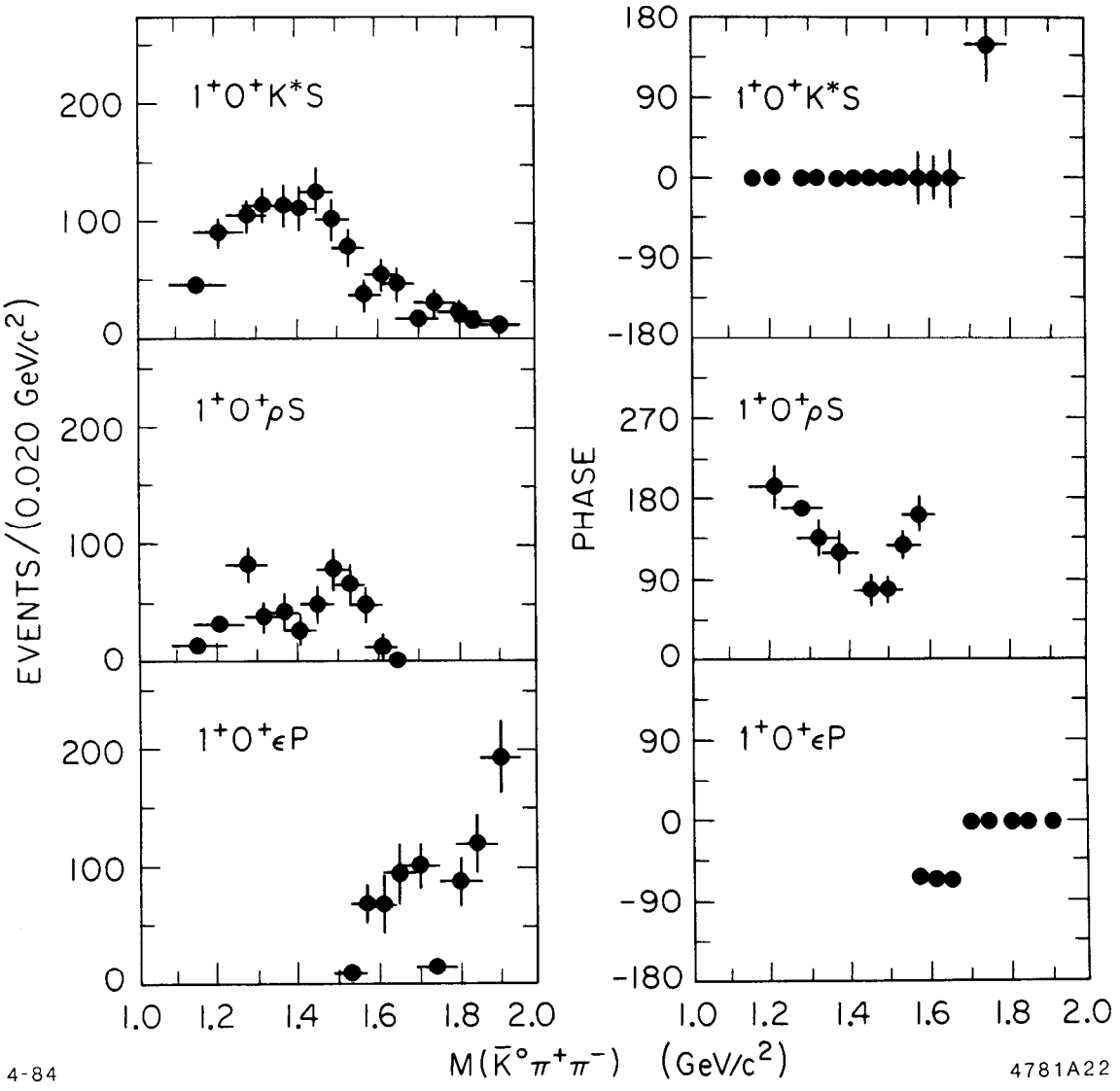
1+0+K*S
1+0+ρS
1+0+εP
EVENTS/(0.020 GeV/c²)
PHASE
M(K̄°π+π−) (GeV/c²)
4-84
4781A22

Fig. 22

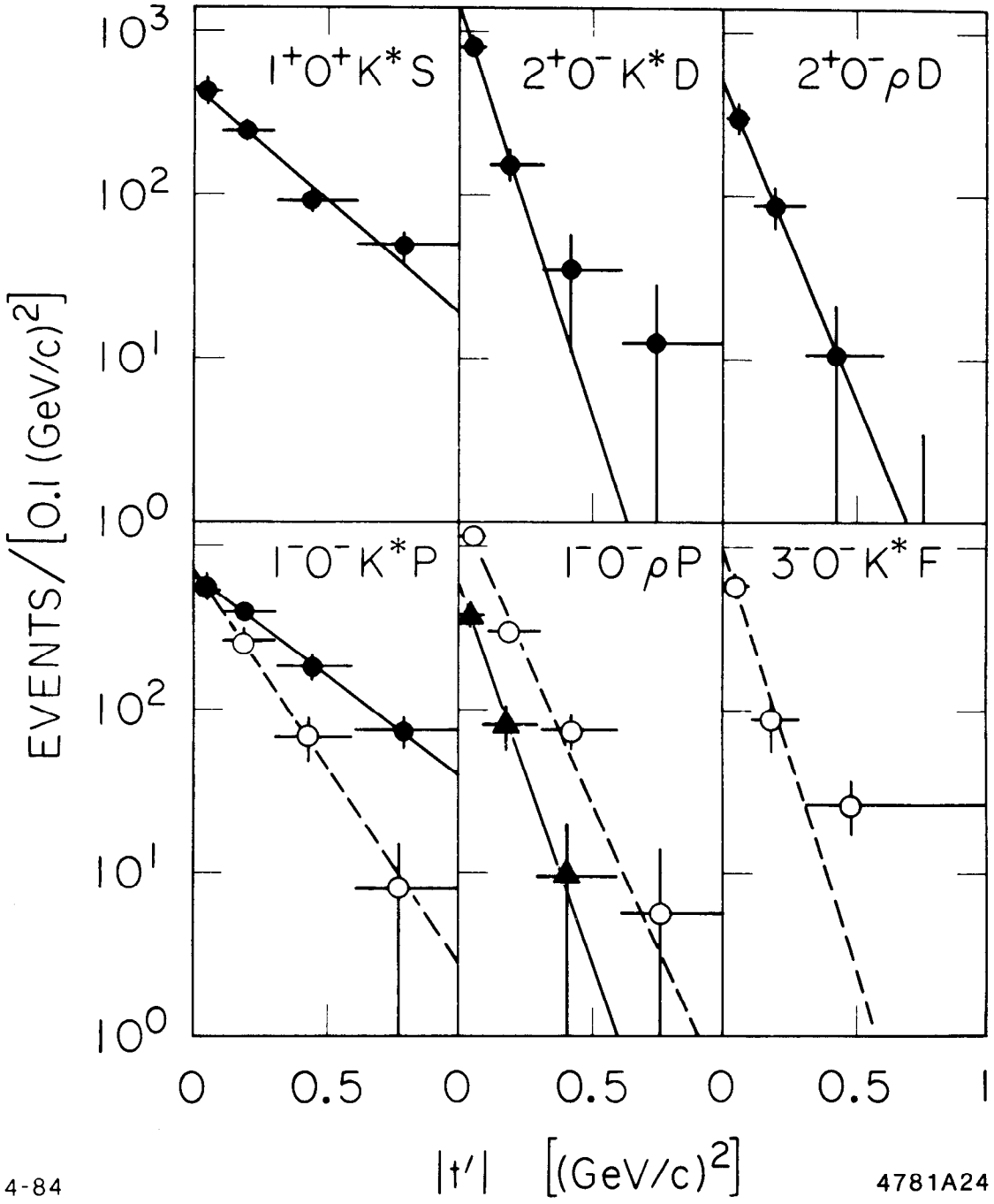
$1^+0^+K^*S$
$2^+0^-K^*D$
$2^+0^-\rho D$
$1^-0^-K^*P$
$1^-0^-\rho P$
$3^-0^-K^*F$
EVENTS/[0.1 (GeV/c)^2]
10^3
10^2
10^1
10^0
0
0.5
1
$|t'|$ [(GeV/c)^2]
4-84
4781A24

Fig. 23